3D models of the circumstellar environments of evolved stars: Formation of multiple spiral structures

Elias Aydi [1,2,3]★ and Shazrene Mohamed[2,3,4,5]★

[1]*Center for Data Intensive and Time Domain Astronomy, Department of Physics and Astronomy, Michigan State University, East Lansing, MI 48824, USA*
[2]*South African Astronomical Observatory, PO Box 9, 7935 Observatory, South Africa*
[3]*Astronomy Department, University of Cape Town, 7701 Rondebosch, South Africa*
[4]*NITheCS National Institute for Theoretical and Computational Sciences, 7701 Rondebosch, South Africa*
[5]*Department of Physics, University of Miami, Coral Gables, FL 33124, USA*

ABSTRACT

We present 3D hydrodynamic models of the interaction between the outflows of evolved, pulsating, Asymptotic Giant Branch (AGB) stars and nearby (<3 stellar radii) substellar companions ($M_{comp} \lesssim 40\,M_J$). Our models show that due to resonances between the orbital period of the companion and the pulsation period of the AGB star, multiple spiral structures can form; the shocks driven by the pulsations are enhanced periodically in different regions as they encounter the denser material created by the substellar companion's wake. We discuss the properties of these spiral structures and the effect of the companion parameters on them. We also demonstrate that the gravitational potential of the nearby companion enhances the mass-loss from the AGB star. For more massive ($M_{comp} > 40\,M_J$) and more distant companions (>4 stellar radii), a single spiral arm forms. We discuss the possibility of observing these structures with the new generations of high-resolution, high-sensitivity instruments, and using them to 'find' substellar companions around bright, evolved stars. Our results also highlight possible structures that could form in our Solar system when the Sun turns into an AGB star.

Key words: stars: AGB and post-AGB – brown dwarfs – circumstellar matter – stars: winds, outflows – planetary nebulae: general.

1 INTRODUCTION

At the tip of the Asymptotic Giant Branch (AGB), stars become unstable to large amplitude, radial pulsations which result in periodic variations in their optical and near-infrared (NIR) light curves on time-scales of the order of ~ 1 to several years (Wood 1979; Feast et al. 1989; Whitelock, Feast & van Leeuwen 2008). These pulsating stars are called Mira variables; they are long period variables that exhibit high mass-loss rates, up to $10^{-5}\,M_\odot\,yr^{-1}$ (Bowen 1988), via slow (3–30 km s^{-1}), cool (100–1000 K) outflows that extend for hundreds of astronomical units.

Detailed understanding of the pulsation mechanism is still lacking, however, it is suggested that they are excited in the convective zone of the star (Freytag & Höfner 2008; Freytag, Liljegren & Höfner 2017; Trabucchi, Mowlavi & Lebzelter 2021). The pulsations are considered an important step in driving the slow, dense Mira winds; layers in the atmosphere are pushed outwards, however, they fall back as they do not have sufficient acceleration to overcome the gravity of the star. The infalling material encounters outward moving material launched by another cycle of pulsation. The collision of these inward and outward moving layers creates shock waves that propagate through the outer atmosphere, lifting the gas far enough away from the star to produce density enhancements that are sufficiently cool

for solid particles, dust grains, to condense (Bowen 1988; Höfner & Olofsson 2018).

Mira variables are known to produce copious amounts of dust in their outflows, usually indicated by a high excess in infrared (IR) emission. The dust plays a role in driving the outflow by mediating between and coupling the stellar radiation field to the gas (Gilman 1972). The dust grains absorb the photon energy, $h\nu$, and the photon momentum, $h\nu/c$, they heat up and start moving outwards. While moving outwards, they collide with and transfer momentum to the gas resulting in a dust-driven wind (Lamers & Cassinelli 1999). An illustration scheme of both processes that drive the outflow is presented in Fig. 1.

State-of-the-art 1D simulations have been able to account for many of the observed properties of Mira outflows described above, such as, their spectra, colours, and mass-loss properties for C-rich Miras (e.g. Nowotny et al. 2013; Eriksson et al. 2014). These time-dependent models have also been used to study how changes in the stellar wind properties produce shell-like circumstellar structures and detached shells observed around AGB stars, as well as linking them to the spherical arcs observed in their progeny, planetary nebulae (e.g. Schoenberner 1981; Kahn & Breitschwerdt 1990; Steffen, Szczerba & Schoenberner 1998; Corradi et al. 2000; Myasnikov et al. 2000; Simis, Icke & Dominik 2001; Schönberner et al. 2005; Mattsson, Wahlin & Höfner 2010).

While asymmetric structures are well-documented and ubiquitous in post-AGB systems and planetary nebulae (Balick 1987; Balick &

★ E-mail: aydielia@msu.edu (EA); shazrene.mohamed@miami.edu (SM)
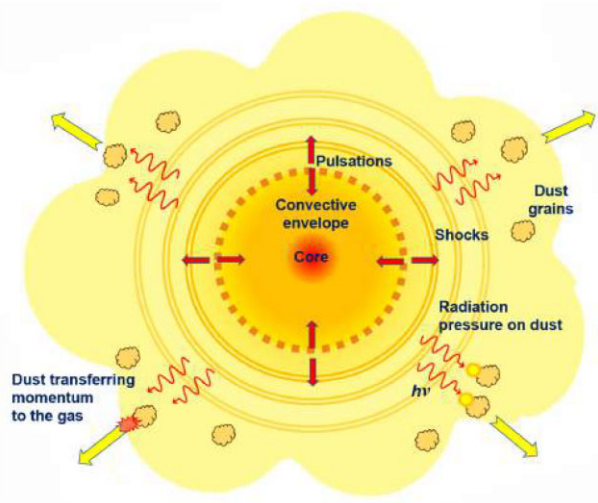
Figure 1. A schematic illustration (not to scale) of the outflow in Mira variables. The pulsation creates shocks in the circumstellar environment driving the outflow (Freytag et al. 2017). While moving outwards, the gas cools down and when its temperature drops below the dust condensation temperature and if the density of the medium is high enough, dust starts to form. The dust grains absorb the radiation from the star, gain momentum, and move outwards, colliding with and transferring momentum to the gas resulting in a slow, dense stellar wind.

Frank 2002; van Winckel 2003; Corradi et al. 2004, 2011; Sabin, Zijlstra & Greaves 2007; Lykou et al. 2011; Ueta et al. 2014; Manick, Miszalski & McBride 2015; Montez et al. 2017), with more recent high resolution, high sensitivity observations, e.g. with the Atacama Large Millimeter/submillimeter Array (ALMA; Wootten & Thompson 2009) and the Spectro-Polarimetric High-contrast Exoplanet REsearch (SPHERE; Beuzit et al. 2019), it has become increasingly clear that deviations from spherical symmetry happen much earlier than previously thought – indeed, while the stars are still on the AGB. Observations of asymmetric structures, e.g. spirals, bipolar outflows, arcs, discs, and equatorial outflows in the circumstellar environments of AGB stars are now commonplace (e.g. Mauron & Huggins 2006; Morris et al. 2006; Olofsson et al. 2010; Lagadec et al. 2011a,b; Maercker et al. 2012; Abate et al. 2013; Ramstedt et al. 2014, 2017, 2020; Starkenburg et al. 2014; Decin et al. 2015; Kim et al. 2015; Lagadec & Chesneau 2015; Doan et al. 2017, 2020; Khouri et al. 2018; Lagadec 2018).

Many of these structures have been linked to shaping by a binary companion, as described by the references above as well as detailed theoretical studies (e.g. Theuns, Boffin & Jorissen 1996; Soker 1998; Mastrodemos & Morris 1999; Balick & Frank 2002; Gawryszczak, Mikołajewska & Różyczka 2002; Nordhaus & Blackman 2006; Mohamed & Podsiadlowski 2007, 2012; Kim & Taam 2012b; Staff et al. 2016; Chen et al. 2017; Saladino & Pols 2019; Saladino, Pols & Abate 2019; Maes et al. 2021; Malfait et al. 2021 and references therein). The C-rich AGB star, R Sculptoris, proved to be a good catalyst for both observational and theoretical studies of the shaping processes (Maercker et al. 2012); having recently undergone a thermal pulse, it is surrounded by a spherical, thin detached shell which was then revealed to harbour a spiral, created by an unseen low-mass companion interacting with the dense AGB outflow. Modelling the high-resolution ALMA data not only improved our understanding of the dramatic changes to the mass-loss properties during a thermal

pulse, but also helped us constrain the properties of the orbiting companion.

Indeed, the high luminosity of AGB stars and the large variations in that brightness caused by their pulsations, make it difficult to detect low-mass companions using radial velocity or transit measurements. However, imaging of the circumstellar environment has been used to infer the presence of planets or substellar companions (e.g. Kervella et al. 2017), and although they are difficult to detect, the number of giant planets detected around evolved stars has increased in the past few years, particularly using radial velocity techniques (e.g. Sato et al. 2003, 2007, 2008; Niedzielski et al. 2007, 2009a,b, 2015; Liu et al. 2008; Gettel et al. 2012a,b; Nowak et al. 2013; Brucalassi et al. 2014; Marshall et al. 2019; Quirrenbach et al. 2019; Jeong et al. 2021; Döllinger & Hartmann 2021); with the majority of these planets at orbital separations ranging from close to intermediate (0.5 to 4.0 AU). Furthermore, Soszyński et al. (2021) suggested that accreting planetary companions – turned brown dwarfs – are the cause of the long secondary periods observed in red giant stars, illustrating the influence of substellar companions on the observed properties of giant stars. However, detailed 3D modelling and predictions of the effects of such close-in substellar companions on the circumstellar envelopes of evolved stars have been lacking.

Struck, Cohanim & Willson (2002) carried out 2D simulations of planets and brown dwarfs in close orbit around Mira variables and they found substantial wakes behind the companion and episodic accretion phenomena, which may give rise to observable optical events and affect SiO maser emission. Kim & Taam (2012b) studied the formation of an Archimedian spiral structure around AGB stars due to the presence of a substellar companion at intermediate distance from the star (10–20 AU), making estimates for the density contrasts between the arm and interarm regions. Using models that included a more detailed treatment of the AGB stellar wind physics, e.g. a sinusoidal piston (at the inner boundary – near the stellar surface), radiative cooling, and silicate dust formation, Wang & Willson (2012) built several 1D models of a pulsating star with a planetary companion in close orbit ($1.019–1.35\,R_*$). Their results showed the formation of multiple spiral arms centred on the AGB star due to the interaction of the planet with the stellar pulsation. The number and period of the spiral arms vary depending on the mass of the companion and its orbital period.

To further aid observational studies, in this paper, we extend the theoretical work of Wang & Willson (2012) to 3D, allowing us to better predict the effect of a close-in companion on the morphology of the outflow at different viewing/inclination angles. Furthermore, unlike previous multidimensional studies where the flow at the inner boundary is prescribed and sets the wind mass-loss properties (e.g. all the previous SPH and grid code models above), in this work we have an outer atmosphere within which the wind launching takes place, allowing us to better study the influence of the companion on the outflow properties as well. In addition, modelling the interaction of close-in substellar companions with a pulsating AGB star could give us insight into the future Solar system, when our Sun turns into a giant, pulsating star. In Section 2, we describe the model setup and numerical details, and the resulting simulations are presented in Section 3. The formation and shaping of the AGB outflow into multiple spirals is discussed in detail in Section 4, and we touch briefly on the observability of these structures, given the sensitivity and resolution of current and future facilities, and the less certain understanding of planet survivability around evolved stars. We conclude with a short summary and highlight potential avenues for future studies in Section 5.

2 NUMERICAL METHOD AND SETUP

2.1 Smoothed particle hydrodynamics

SPH (Gingold & Monaghan 1977; Lucy 1977; Monaghan 1992) is a Lagrangian method where the fluid is discretized into a finite number of particles. Each particle has fluid properties, such as density, velocity, pressure, and internal energy. Starting from an estimate of the density obtained by summing and smoothing the masses of neighbouring particles, the other properties are derived using the Lagrangian formulation of the fluid equations. For the interpolation in this case we use a cubic spline smoothing kernel. The method conserves momentum, energy, entropy, and angular momentum by its Lagrangian construction (Springel & Hernquist 2002). Artificial viscosity is added in order to model shocks and density discontinuities, where the viscous forces are added to the equation of motion as an excess of pressure on the particles (Monaghan & Gingold 1983; Balsara 1995).

We use the SPH cosmological simulation code GADGET-2 (Springel 2005), which is a TreeSPH code that is capable of following a collision-less fluid with the *N*-body method and an ideal gas by means of SPH. The gravitational forces and self-gravity in GADGET-2 are derived by the use of a hierarchical Barnes–Hut (BH) oct-tree algorithm (Barnes & Hut 1986).

2.2 Model setup

2.2.1 Modelling the pulsation and atmosphere

The stellar pulsations are thought to originate in the convective zone of the AGB star (see e.g. Freytag et al. 2017). These pulsations result in shock waves that travel through the extended atmosphere and begin to drive the outflow. Our models adopt the approximation from Bowen (1988), where the pulsation is simulated by an artificial piston (in this work, a shell of particles) placed at the edge of the photosphere ($R_{piston} \sim 0.92\,R_{photo}$). The artificial piston, placed directly below the atmosphere of the star, oscillates sinusoidally starting from a maximum amplitude U_{amp}. The piston acts like a boundary layer where the radius and velocity of the boundary vary with time as follows:

$$R = R_0 + U_{amp}(P/2\pi)\sin(2\pi t/P_{puls}),\qquad(1)$$

$$U = U_{amp}\cos(2\pi t/P_{puls}),\qquad(2)$$

where R and U are the piston radius and velocity at time t, respectively, R_0 is the initial radius of the piston, U_{amp} is the piston velocity amplitude, and P_{puls} is the pulsation period.

The fundamental pulsation mode, P_{puls} is derived from the period–mass–radius relationship of Ostlie & Cox (1986) which relates the P_{puls} to the mass (M_*) and radius (R_*) of the star through:

$$\log P_{puls} = -1.92 - 0.73\log M_* + 1.86\log R_*.\qquad(3)$$

The atmosphere of the star is represented by another shell of gas particles, just above the artificial piston. We use equal mass particles ($\approx 7.476 \times 10^{21}\,\mathrm{g} \approx 3.75 \times 10^{-12}\,\mathrm{M_\odot}$), set in a $1/r^2$ density distribution. The combined mass of the artificial piston and atmosphere is not included in the mass of the central star. A density distribution of $1/r^2$ agrees well with the observations (Struck et al. 2002); using an exponential density profile similar to the one from Wang & Willson (2012) would be preferable, however, such a distribution is difficult to achieve in SPH models using equal mass particles. The inner regions of the star are not modelled and instead a point mass (particle) is used to simulate its gravity. The standard

Table 1. Standard model parameters.

|	
M_*	$1\,\mathrm{M_\odot}$
R_*	$268\,\mathrm{R_\odot}$
P_{puls}	394 d
U_{amp}	$4\,\mathrm{km\,s^{-1}}$
T_{eff}	2966 K
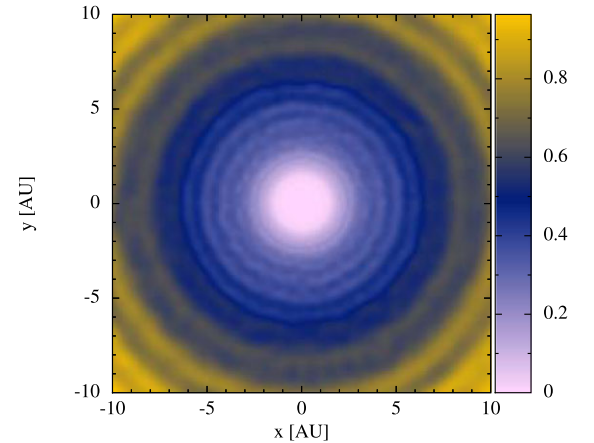
Figure 2. A rendered cross-section of the smoothing length, h, of each particle near the atmosphere of the star.

parameters of the central star used in all our models are listed in Table 1.

2.2.2 Numerical resolution and smoothing

Our models consist of 4.2×10^6 gas particles; 9.2×10^5 particles for the piston and 3.3×10^6 particles in the atmosphere of the star. Each gas particle has a mass of $\approx 7.476 \times 10^{21}\,\mathrm{g} \approx 3.75 \times 10^{-12}\,\mathrm{M_\odot}$. The star and the companion are added to the model as Gadget-2 'star' (point-mass) particles with masses equal to M_* (see Table 1) and M_{comp} (see Table A1), respectively.

The smoothing length, h in SPH simulations defines the scale over which the fluid properties of the particles are interpolated. Therefore, h effectively determines the resolution of a simulation. To achieve the goals of the Lagrangian adaptivity in SPH, GADGET-2 allows the smoothing length of each particle to vary in both space and time. Hence, the resolution increases in high-density regions (e.g. where shocks are forming from the stellar pulsation or interaction of the stellar wind with the companion) and decreases in low density regions. In Fig. 2 we show a cross-section plot around the regions of the periodic shock-wave formation, showing that for the ≈ 4 million particles we use, the smoothing length is $\lesssim 0.8$ AU.

2.2.3 Modelling the radiation pressure on dust

The radiation pressure on dust results in a net outward acceleration of the dust grains that then transfer momentum to the gas by collision. Dust formation is typically modelled via two approaches, the so-called moment method (Gail & Sedlmayr 1988; Gauger, Sedlmayr & Gail 1990), which effectively calculates the growth of dust grains, assuming the formation via primarily single *monomers*, such as C, SiO, and Fe. The other method is the chemical kinetic approach, which was introduced by Cherchneff (2006) and in which the chemistry of dust formation is described by using a chemical kinetic

network of reactions. These approaches work successfully for C-rich AGB stars where a dust-driven wind is achieved, however, for O-rich AGB stars the nucleating species are still uncertain and pre-existing grain seeds are used to initiate the process and trigger a dust-driven wind (Höfner 2008; Bladh & Höfner 2012; Bladh et al. 2013). There are also uncertainties regarding the grain composition (Bladh et al. 2013) and the Fe-enrichment needed to reproduce the observable features (Höfner et al. 2021).

Given these uncertainties, and the significant numerical cost to follow this in detail, similarly to Wang & Willson (2012), we adopt the simplified method from Bowen (1988) to model dust formation. The approach consists of comparing the radiative equilibrium temperature (T_{eq}) of the gas to the condensation temperature (T_{cond}) of the dust. If T_{eq} is less then T_{cond} an acceleration is added to the gas particles. As detailed radiative transfer is not included in our models (due to computational cost), we assume radiative equilibrium (Lamers & Cassinelli 1999):

$$T_{eq} = T_{eff} \left(\frac{R_*}{2r} \right)^{\frac{2}{4+p}}, \tag{4}$$

where r is the radius of the gas from the central star and p is a power-law coefficient adopted from Bladh & Höfner (2012) for different types of dust grains. We experiment with both silicates and carbonaceous grains. For the silicate (Mg_2SiO_4) grains, we use a dust condensation temperature $T_{cond} = 1100$ K and $p = -0.9$. For amorphous carbon (amC) grains, we adopt $T_{cond} = 1500$ K and $p = 2.1$. A more realistic approach to calculate the optical depth in the cirumstellar medium and the equilibrium temperature of the gas will be presented in a future work.

The dust cross-section for radiation pressure, in $cm^2 \, g^{-1}$ of gas is derived using:

$$k_D = k_{max} \frac{1}{1 + \exp[(T_{eq} - T_{cond})/\delta]}, \tag{5}$$

where δ is the parameter for the condensation temperature range and the maximum cross-section per unit mass k_{max} is specified as an input parameter. A value of $k_{max} = 1.5 \, cm^2 \, g^{-1}$ is chosen to maintain the ratio between the acceleration due to the radiation pressure on dust and the gravitational acceleration, $\frac{dv}{dt}(rad)/\frac{dv}{dt}(g)$, less than or equal to 0.95 (Bowen 1988).

The acceleration of the gas particles due to the radiation pressure on dust, which is added to the particles acceleration is defined as follows:

$$\frac{dv}{dt}(rad) = \frac{k_D L}{4\pi r^2 c}, \tag{6}$$

where L is the luminosity of the star, r is the distance between the gas particle and the star, and c is the speed of light.

Our models do not take dust destruction into account for several reasons: (1) The formation of dust occurs beyond ~ 2–$3R_*$ (~ 2–4 AU), (2) The hot shocks that lead to dust destruction occur below $\sim 2R_*$, (3) Our assumption of adding acceleration to the gas particles considers instantaneous dust formation depending on T_{eq}, and the shock waves generated by the pulsation every pulsation period do not reduce significantly the dust abundance (Wang & Willson 2012).

2.2.4 Cooling

Cooling or thermal relaxation by radiative transfer is not included in this work. The models are all adiabatic such that the net radiative energy per unit mass gained/lost, Q, is always equal to zero. The results from these models produces realistic mass-loss rates on the

order of $\sim 10^{-7} \, M_\odot \, yr^{-1}$ without including dust formation. Note that the Bowen (1988) models with adiabatic processes resulted in high mass-loss rate, but his results were less catastrophic than the models of Wood (1979). More realistic cooling, such as relaxation towards T_{eq} at a finite rate will be implemented in future versions of the code.

2.2.5 The orbit of the companion

The substellar companion is placed in a circular orbit around the pulsating star. The companion orbits in the equatorial/orbital plane (the x–y plane) and is added as a point-mass particle. The orbit of the companion is not affected by tidal drag or mass-loss in this version of the model. The companion is assumed not to accrete any material due to: (1) the relatively small mass of the companion compared to the mass of the star, (2) the short time-scale of the simulation compared to the accretion time-scale in case of a substellar companion (see e.g. Villaver & Livio 2009).

For models where the companion is at an orbital distance of $d_{comp} < 3R_*$ from the centre of the AGB star, it is considered in circular orbit around the centre. The star is then kept stationary, particularly since the barycentre of the system is very close to the stellar centre (separated by $\leq 0.06R_*$). In models where $d_{comp} > 3R_*$, the star and the companion are both orbiting the barycentre of the system which lies within the radius of the star for most of the models. For such models, the stellar centre is separated by ~ 0.1–$1.0R_*$ from the barycentre of the system. d_{comp} is always the distance between the companion and the centre of the star. In Appendix A, we elaborate on how the properties of the companion, such as, the relative velocity (v_{orb}), orbital period (P_{orb}), angular momentum L, and d_{comp} were derived. In some models, we intentionally fix some of the properties of the companion to test the effect of changing other properties.

3 RESULTS

Our results consist of a set of 40 models. The variables in these models are the P_{orb}, d_{comp}, the mass of the companion (M_{comp}), U_{amp}, and the resonance mode $M:N$ (for every N pulsation cycles, the companion completes $\sim M$ orbits). Note that for these resonances M is always $< N$ and N is equal in number to the number of spiral structures (N_s). The resonance mode represents the P_{orb}–P_{puls} resonance. Table A1 lists all the models with their different parameters. Models 1 to 32 led to the formation of multiple structures ($N_s \geq 2$). However, models 33 to 40 led to the formation of one dominant spiral arm ($N_s = 1$). In all the models $P_{puls}/P_{orb} \approx M/N < 1.0$. Systems where this ratio is larger than 1.0 are beyond the scope of this study and are excluded from our analysis. In such systems, P_{orb} is smaller than P_{pul} (394 d) implying that the companion is below the photosphere and hence it is already completely engulfed. For computational efficiency, models 1 to 40 do not include acceleration due to radiation pressure on dust. The effect of this process is studied with a small subset of models and we present the results in Section 3.7.

3.1 Formation of periodic shock waves

The stellar pulsation creates a cycle of shock waves that travel outwards carrying material away from the star. These shocks form when the outgoing material (due to the pulsation) meets with the in-falling material (due to the gravitational potential of the star). At the shock formation region, the temperature of the gas increases up
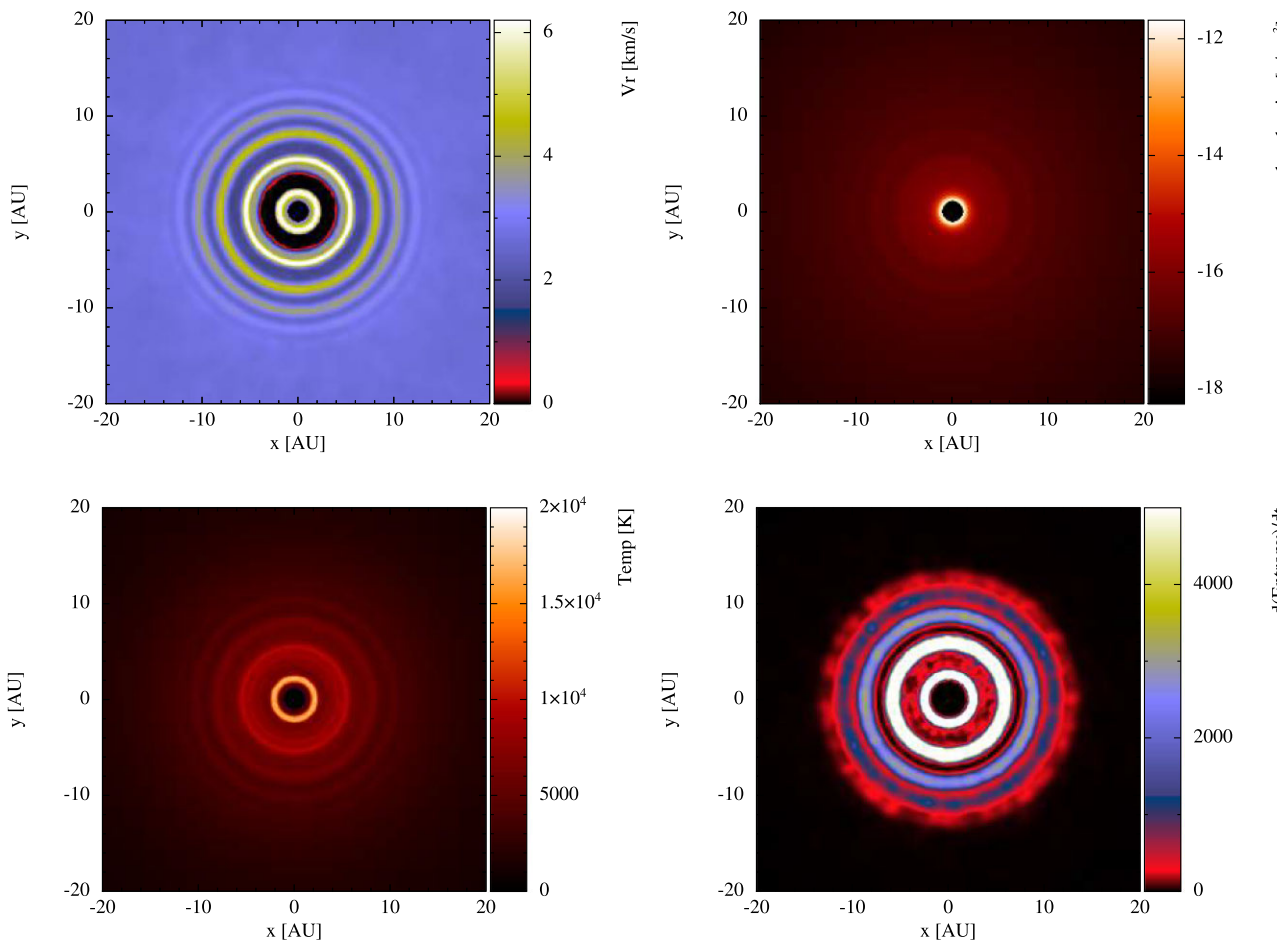
Figure 3. Cross-section slices through the orbital plane x–y of a single star, showing radial velocity, density, temperature, and entropy, from top left to bottom right, respectively. The plots show the formation of circular shock waves in 2D (spherical shells in 3D) due to the stellar pulsation.

to $\sim 1.5 \times 10^4$ K and the gas velocity attains $\approx 6-10\,\mathrm{km\,s^{-1}}$. As the shocks propagate outwards, they decelerate and cool down.

In the case of a single star, the shocks produced by the radial, sinusoidal motion of the piston are spherically symmetric. In Fig. 3 we show cross-sections through the orbital plane of different gas parameters for a single star (model 0). The assumption of spherical symmetry for the piston and shock excitation is idealized (see e.g. Freytag & Höfner 2008; Freytag et al. 2017). The detailed models of Freytag et al. (2017) show that convection cells and fundamental-mode pulsation will result in chaotic shock wave structures around the AGB star, shifting from spherical symmetry. However, they also show that if the radial velocity is averaged over a sphere around the star, radial periodic shock waves are clearly visible (see fig. 5 in Freytag et al. 2017). We will elaborate more in Section 4 on the implications of this assumption for our results.

The interpolation at the heart of SPH means that sharp discontinuities require large numbers of particles (high resolution) to minimize the smoothing region. Although limited due to computational expense, we explore the effect of changing the resolution on the formation of the radial shock waves. We simulate a single star with 2.1×10^5 and 1.1×10^6 particles. In Fig. 4, we show radial velocity cross-sections from these two simulations. The shock waves are better resolved for higher resolution simulations as expected. Obviously, the increase in the resolution allows for better estimation of the gas properties near discontinuities. In the simulation with the lowest resolution (2.1×10^5 particles), the radial periodic shock waves are barely resolved.

We also test the effect of including the acceleration due to radiation pressure on dust grains on the outflow structure and morphology. In these simulations we use only 1.1×10^6 particles to reduce the computational time. In Fig. 5 we show radial velocity cross-sections and radial velocity profiles for a single star with acceleration due to radiation pressure on silicate and amorphous carbon grains (see Fig. 4-left-hand panel to compare with the model that does not include dust formation). With the addition of dust acceleration, the outflow velocity of the gas increases, as expected. The gas velocity within the shock region increased by a factor of around 2, when adding dust compared to the model without dust. Both models, with Si-based dust grains or amC based dust grains result in similar gas velocity excess. In Fig. 5 we also present the radial acceleration due to dust as a function of radius. Our values are comparable to those presented in fig. 2 of Wang & Willson (2012).

3.2 Formation of multiple spiral structures

If the companion is at a $d_{\mathrm{comp}} < 3R_*$ and if there is a resonance between P_{orb} and P_{puls}, multiple spiral structures form in the circumstellar environment centred at the AGB star and extending for more than 70 AU. To elaborate on how these structures form, we choose model 9, where P_{orb} is in a resonance mode of around 1:2
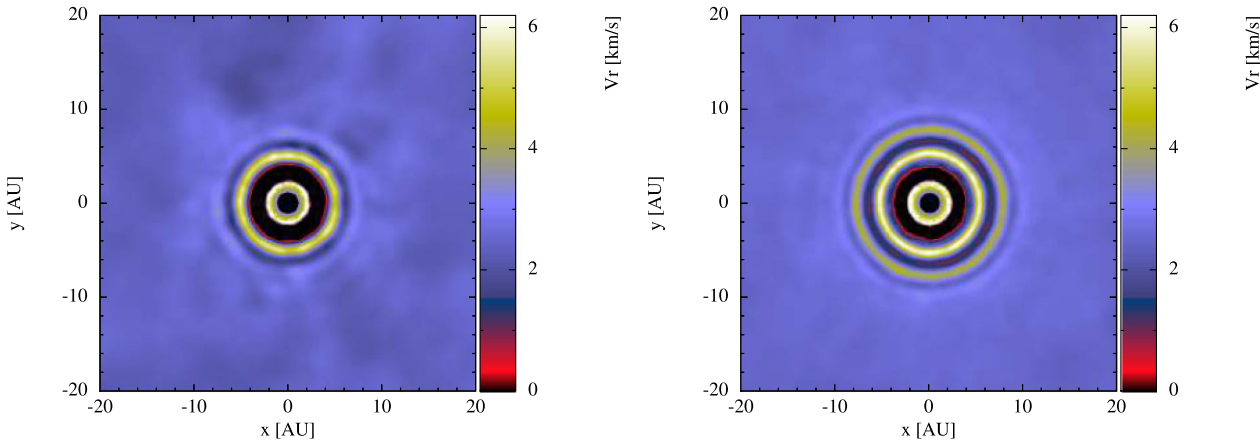
Figure 4. Radial velocity cross-sections through the orbital plane x–y of a single star, using 2.5×10^5 particles (left-hand panel) and 1.1×10^6 particles (right-hand panel).
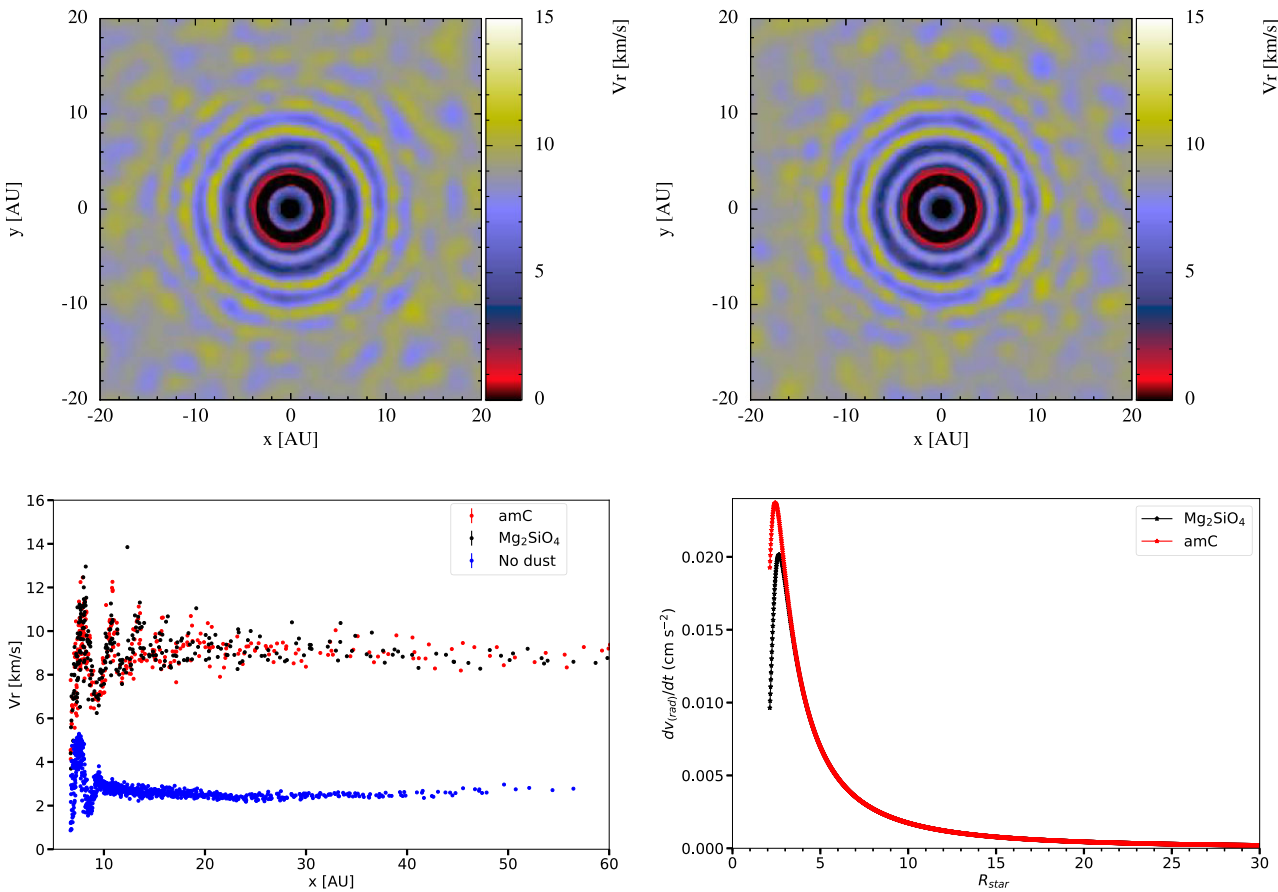

Figure 5. Top: 2D radial velocity cross-section slices through the orbital plane x–y of a single star after ≈ 76 pulsation cycles, with silicate based dust (left-hand panel), and with amorphous carbon dust (right-hand panel; see the right-hand of Fig. 4 for comparison with a single star without dust). Bottom left-hand panel: radial velocity profiles along the *x* direction for $-2 < y\,(\mathrm{AU}) < +2$. We remove the particles which constitute the atmosphere of the star to focus on the V_r profile and shock waves. Bottom right-hand panel: the radial acceleration due to radiation pressure on dust, against radius, for silicate-based (Mg_2SiO_4) and amorphous carbon-based (amC) dust, as derived using the formalism and assumptions made in the code.

with P_{puls}, as an example, and note that the same interaction process occurs in the formation of multiple spiral structures in models 1 to 32 (Table A1).

While the companion is traveling in the dense circumstellar medium around the star, its gravitational potential creates a wake that trails behind it. A 2D temperature cross-section slice through the

orbital plane [panel (a) in Fig. 6] shows the wake of the companion, consisting of a 'leading arm' denoted arm (1) and a 'trailing arm' (inner arm) denoted arm (2). Due to the close-in circular orbit of the companion, and the resulting high orbital velocity, the two arms have different degrees of curvature, with arm (1) being more curved than arm (2).
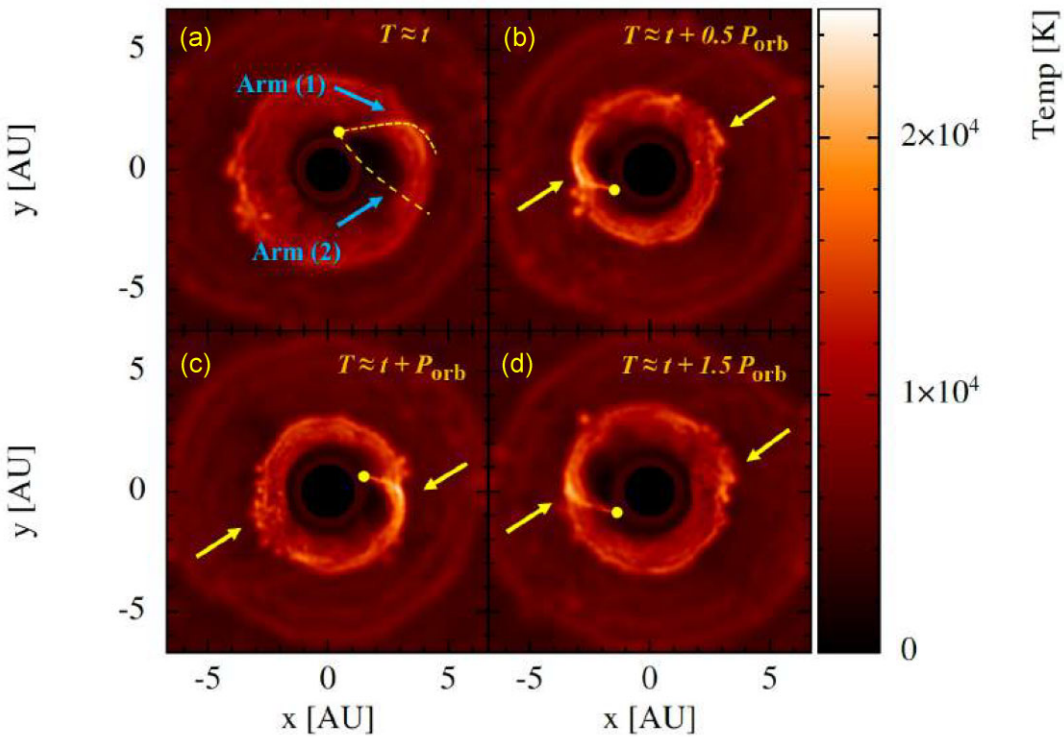
Figure 6. 2D temperature cross-section slices through the orbital plane from model 9. Panel (a) shows the companion traveling in the dense circumstellar environment creating a wake behind it consisting of two arms, a leading arm denoted (1) and a trailing arm denoted (2). The companion position is identified by a yellow point and the arms are highlighted with dashed yellow lines for guidance. Panel (b) shows two shocks (indicated by the blue arrows) forming due to the interaction of arm (1) with the shock wave on the left-hand side, and the tail of arm (2) with the same shock wave on the right-hand side of the orbital plane. Panel (c) is same as (b) but after $\sim$ 1 pulsation cycle (half an orbital period). Panel (d) is same as (b) but after $\sim$ 2 pulsation cycles (one orbital period). The shocks on both sides cluster to form two spiral arms centred on the AGB star.

Due to its proximity to the star and the shock formation region, the companion exerts a gravitational pull on the upper atmosphere of the star. This increases the velocity and temperature of the pulled gas below the companion, enhancing the mass-loss locally (see e.g. Wang & Willson 2012). When the upcoming shock waves due to the stellar pulsation meet the wake of the companion, they lead to a strong shock, propagating outwards. Particularly, these shocks occur between the shock waves and arm (1) of the wake [blue arrow in panel (a) of Fig. 6]. At the location of these shocks, the gas temperature rises up to $\approx 3 \times 10^4$ K and the gas velocity increases up to ≈ 18 km s^{-1}. Compared to its surrounding medium, the shock velocity and temperature are a factor of 3 greater.

After half an orbit, arm (1) of the wake meets a subsequent pulsation cycle, which creates another shock on the other side of the orbital plane [yellow arrow in panel (c) of Fig. 6]. This repeats with every half orbit and each pulsation cycle. Similar shocks occur between the tail of arm (2) and the stellar pulsations [e.g. yellow arrows in panels (b), (c), and (d) in Fig. 6]. These shocks cluster on each side of the orbital plane to form two spiral structures, centred on the AGB star, with a long-lasting momentum. The high velocity of the shocks lead to a velocity contrast with the surrounding medium.

Since, the ratio between $P_{\rm puls}$ and $P_{\rm orb}$ in model 9 is $\simeq 0.48$ (slightly offset from $M/N = 0.5$), this means that the companion meets the shock waves at a slightly earlier location every new pulsation cycle. This is the reason behind the formation of dynamic spiral structures instead of two static bars. We will elaborate more on the formation of static bars in Section 3.3.

In Fig. 7, we show a sample of multiple spiral structures/bars from models 4, 9, 21, and 26. The plots are radial velocity cross-sections through the orbital plane. In each of these models, a certain number of spiral structures (or bars) form around the system depending on the resonance between the orbital and pulsation periods. A time-evolution visualization of the models can be found in the supplementary material.

Our models show spiral structures in the velocity cross-sections, however, the spirals are not clearly resolved in the density cross-section plots (see Fig. B1). This is because the density at the shock location is not substantially different compared to the surrounding medium. An increase in the resolution of the simulation might allow us to better resolve the gas properties at the shock location and therefore resolve the spiral structures in the density cross-section. In addition, implementing more realistic cooling regimes will increase the density contrast at the shocks. The 1D models of Wang & Willson (2012) show multiple spiral arms in the density cross-sections. This again emphasizes that implementing realistic cooling and increasing the resolution of the simulation are necessary to resolve the spirals in the density plots.

Fig. 8 presents a comparison of radial velocity, temperature, and density profiles along the x-axis from models 0 (no companion) and 9, after $\simeq 90$ pulsation cycles. We choose to show the profiles after 90 pulsations because at this stage the second winding of the spiral arm is parallel to the y-axis, which allows a better representation of the spiral arms in the profiles. The radial velocity profiles are drastically different between the two models. In model 0, the velocity profile shows the stellar pulsations only. However, in model 9, the velocity profile shows (1) the stellar pulsation, which appear as rapid oscillations over short distances ($\sim$ 2–3 AU) and (2) the spiral structures which appear as global oscillations over the extent of the
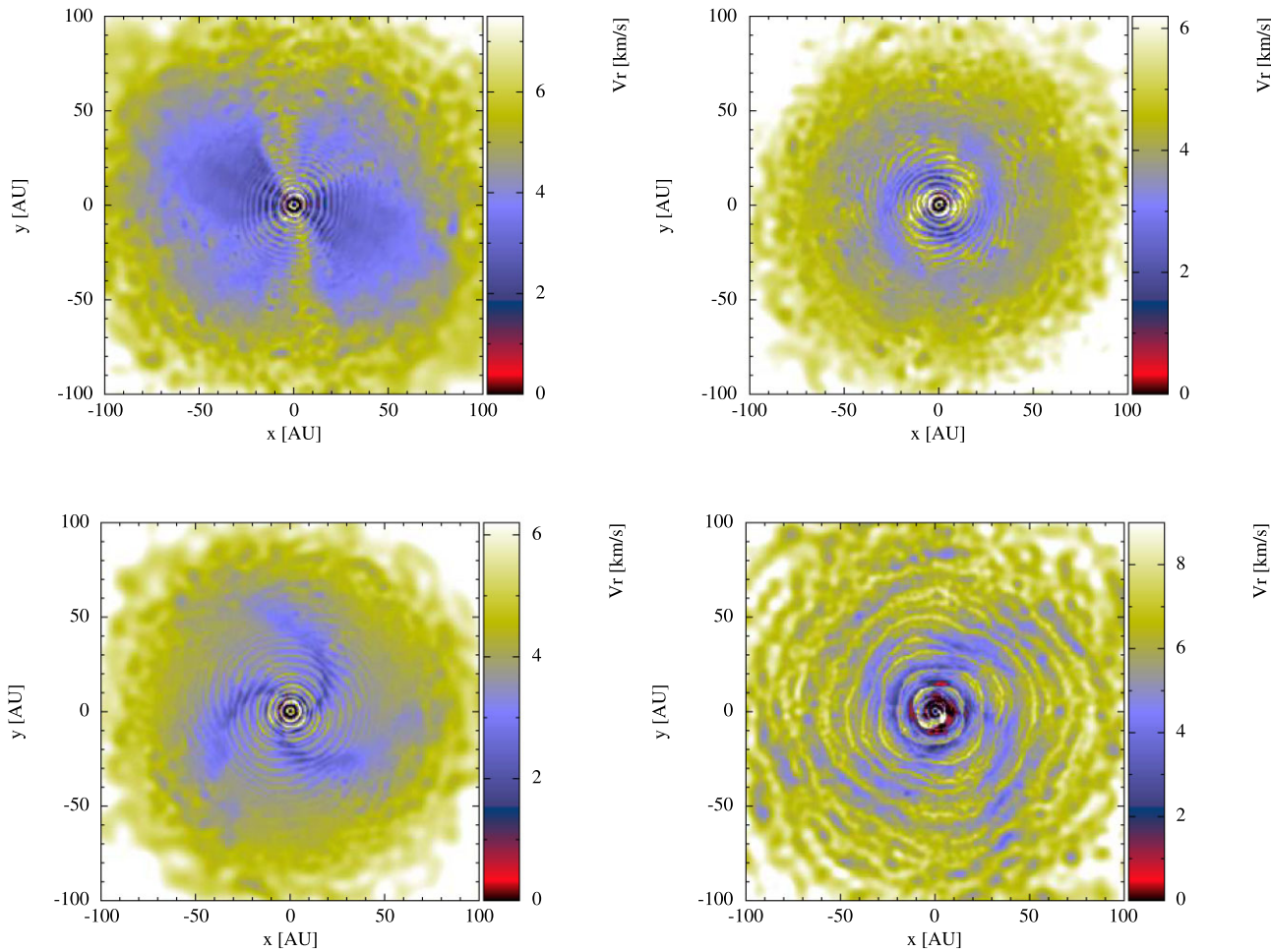
Figure 7. Velocity cross-sections through the orbital plane after ∼ 76 pulsation cycles for models 4, 9, 21, and 26, showing the different morphology and numbers of spiral structures depending on the resonance mode between the pulsation and orbital periods. Top left-hand panel: model 4 showing two static bar-like structures due to a resonance exactly equal to 1:2. Top right-hand panel: model 9 showing two spiral structures due to a resonance ≈ 1:2. Bottom left-hand panel: model 21 showing three spiral structures due to a resonance ≈ 1:3. Bottom right-hand panel: model 26 showing four spirals due to a resonance ≈ 1:4.

circumstellar medium. Overall, the spiral structures show a velocity contrast of a factor of ≈ 2.0 compared to the medium between the spirals. This distinction between models 0 and 9 is not very obvious in the temperature and density profiles, however, there are still major differences between the two models and the shocks between the stellar pulsations and the companions are clearly visible in the profile as temperature and density gradients, particularly between 15 and 35 AU, which is consistent with the location of the spiral arm. This indicates the presence of spiral structures in the density profiles but the contrast with the surrounding medium is low, which is the reason these spirals are not resolved in the density cross-sections.

In Fig. B2, we show entropy cross-sections for models 9. The two spiral structures are resolved in the entropy cross-section, which emphasizes that the multiple spiral structures are indeed present and are the outcome of clustered shocks between the stellar pulsations and the wake of the companion.

If there is no P_{orb}–P_{puls} resonance, the shocks between the wake of the companion and the pulsations occur at different locations in the orbital plane leading to a random distribution of shocks around the AGB star, hence neither evident spirals nor bars form (see Fig. 9).

3.3 Properties of the spiral arms

The multiple spiral arms forming around the AGB star in the orbital plane are Archimedean spirals propagating in the radial direction. The spirals have the following properties:

(i) **Number and period of the spiral arms:** the number of spiral arms, N_{s}, is directly correlated with the resonance mode and hence with P_{orb} and P_{puls}. For a resonance mode M:N, the number of spiral arms is always equal to N. We consider the spiral arm period (P_{sa}) as the period of the spiral pattern. It is the time for which the spiral pattern repeats itself. In the case of two spiral arms, the period is one half of a full apparent rotation of a spiral arm. In the case of three spiral arms, the period is one third of a full apparent rotation. Wang & Willson (2012) derived a relation between the P_{sa}, P_{orb}, P_{puls}, and N_{s} based on their models and some analytic considerations. We find the same relation based on our models. For $N_{\mathrm{s}} > 1$, P_{sa} is derived using:

$$P_{\mathrm{sa}} = \frac{P_{\mathrm{orb}} P_{\mathrm{puls}}}{\left| M P_{\mathrm{orb}} - N P_{\mathrm{puls}} \right|}, \tag{7}$$

where M and N represent the resonance mode M:N. In Table A1 we list P_{sa} for all our models.
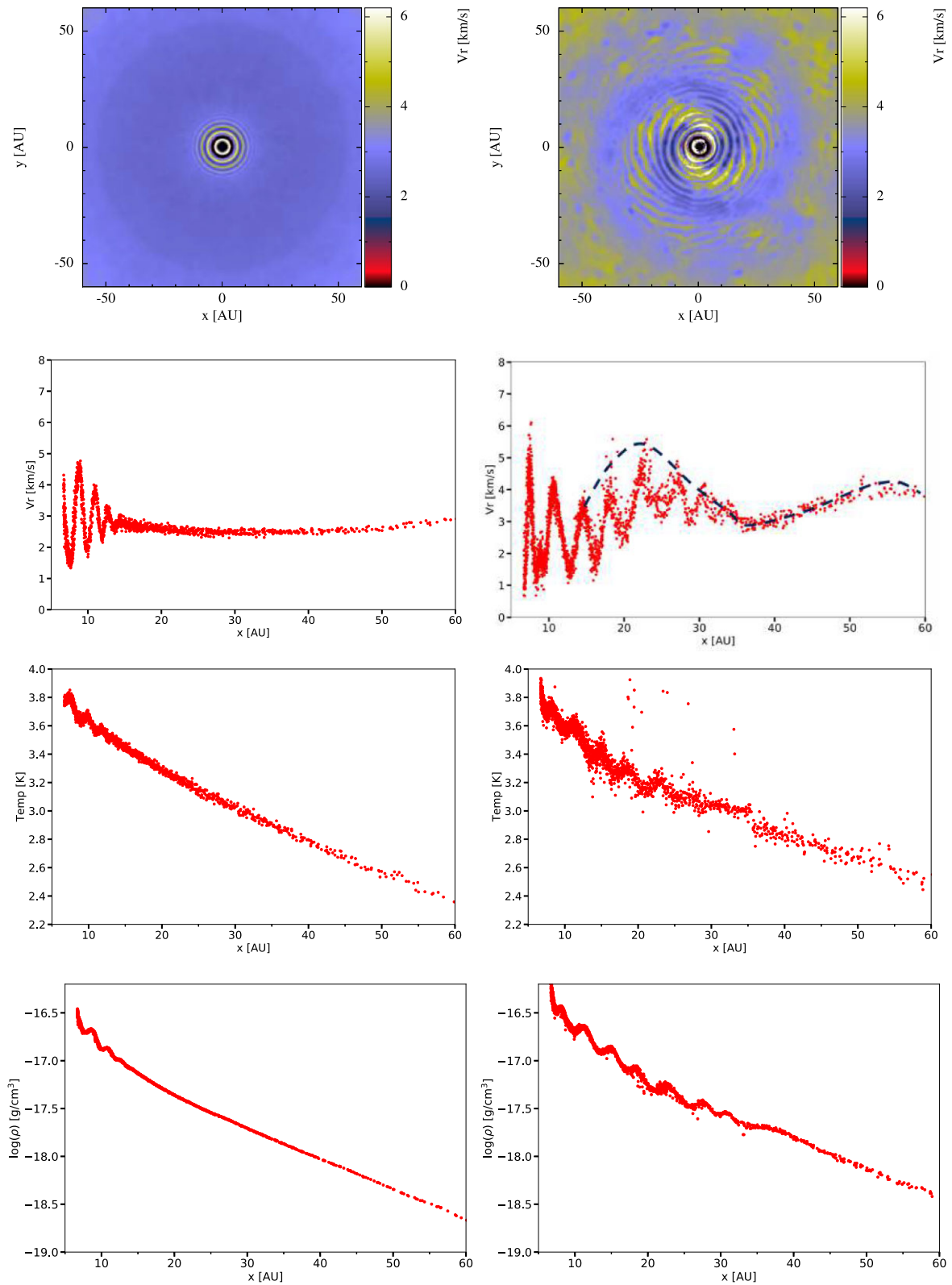
Figure 8. From top to bottom: radial velocity cross-section and radial velocity, temperature, and density profiles from models 0 (left-hand panel) and 9 (right-hand panel) after ≈ 90 pulsation cycles, along the *x* direction for −2 < *y* (AU) < +2. We remove the particles which constitute the atmosphere of the star to focus on the V_r profile and spiral structures. We add a blue dashed line for guidance to help the reader track the spiral structure location.
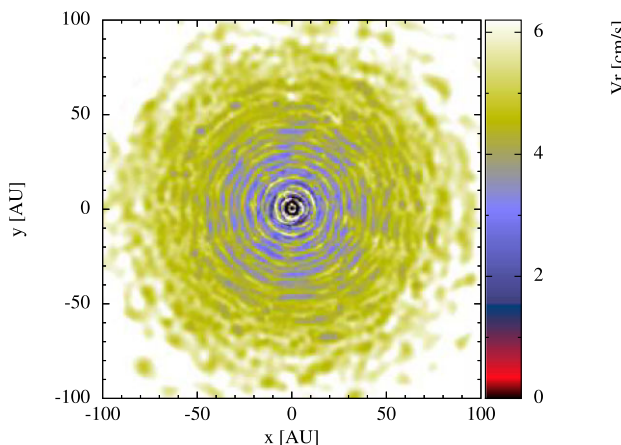
Figure 9. Radial velocity cross-section through the orbital plane, after ≈ 76 pulsation cycles, from a model that exhibits no $P_{\rm orb}$–$P_{\rm puls}$ resonance ($P_{\rm orb}$ = 1044 d). The shocks do not cluster and hence no spiral structures form.

(ii) **The winding of the spiral arms:** depending on the orbital period of the companion, the spiral structures show faster or slower winding. We discuss this thoroughly in Section 4.3. Fig. B3 represents radial velocity cross-section plots of different time-steps from model 9, which shows the winding of the spiral arms with time. The arms appear to be merging and fading at larger distances, however, given that the spirals are moving radially, we do not expect them to completely merge. The apparent merging and fading of the arms is a numerical effect due to the limited number of particles in our simulations. Injecting more particles in the simulation should maintain the spiral structures over a longer time-span. In addition, our simulations show fading shocks/spirals at distances larger than 70 AU. This is expected given that the shocks are spreading over larger distances in a region of low resolution, near the boundaries of our simulations. Similarly, Gawryszczak et al. (2002) carried out SPH simulations of AGB stars in close binary systems. Their models result in the formation of a single spiral structure due to the orbital motion of the secondary star. In these models they estimate the diffusion (dissipation) radius (r_d) and time-scale (t_d) of the spirals due to density gradient at the boundary of their simulations to be $r_d = t_d \times v_w = P_{\rm orb} \times v_w^2/c$, where v_w is the wind velocity and c is the local sound speed. However, they also note that due to the decrease in the resolution of the simulation and increase in the smoothing length at its boundary, the dissipation radius of the spirals becomes much smaller than the predicted one and is dominated by the numerical dissipation.

(iii) **Equation of motion of the spirals:** although they appear to be rotating in a specific direction, the shocks forming the spiral arms propagate in the radial direction. The apparent rotation of the spiral pattern and the winding of the spiral arms are due to the offset between ratio of $P_{\rm puls}/P_{\rm orb}$ and M/N. The shocks cluster into spiral arms that propagate in the radial direction with a speed (V_s) depending on the $M_{\rm comp}$, $U_{\rm amp}$, and the local sound speed. The local adiabatic sound speed is density dependent and it is expressed as $c_s^2 = \gamma\, p/\rho = \gamma(\gamma - 1)e$ with γ being the adiabatic index, e the gas specific internal energy, ρ the gas density, and p the gas pressure. The gas Mach number ($M_{\rm gas}$) is then derived by dividing the gas radial velocity by the local sound speed: $M_{\rm gas} = V_r/c_s$. The Mach number of the spiral structure (M_s) is equal to $M_{\rm gas}$ at the location of the spirals (where the shocks sweep through the gas). In Fig. B4, we plot the Mach number of the gas for models 1 to 12, after $\simeq 76$ pulsation cycles. In most of the models, the spiral arms show supersonic

speeds. From our models and analytical considerations, we derive the following equation that describes the equation of motion of the spiral arms:

$$r(t) \sim 2\,\theta(t)\,V_s(r, t)\,d_{\rm comp} + d_{\rm comp},$$

where $r(t)$ defines the radial position of a section of the spiral arm at time t and $\theta(t)$ is equal to $(t/P_{\rm sa})\pi$.

(iv) **Formation of bars:** if the ratio of $P_{\rm puls}/P_{\rm orb}$ is $\simeq M/N$ (e.g. model 3, 4, 5), the shocks cluster into bar-like structures instead of dynamic spiral arms (see top left-hand panel of Fig. 7). For such models, the shocks between the pulsation and the companion's wake occur at almost the same location during every pulsation cycle. If the ratio of $P_{\rm puls}/P_{\rm orb}$ is exactly equal to M/N, the bars are static (e.g. model 4), however, if it is slightly greater or smaller, the bar-like structures are then dynamic, but their period is very long and they eventually turn into spiral arms on a time-scale of the order of $\simeq P_{\rm sa}$ (e.g. model 5; see Section 4.3).

3.4 Observing the system at different viewing angles

One of the advantages of 3D modelling is the ability to observe the system in different directions. Cross-section slices through the polar planes, (z–x) and (z–y), do not show spiral structures, instead they show complex structures, such as arcs and bars around the system (Figs B6 and B7). The formation, morphology, and symmetry of these structures depends on the resonance between $P_{\rm puls}$ and $P_{\rm orb}$.

To describe the formation of these arcs and bars, we will adopt model 9 again as an example. The wake of the companion resembles a cone-like-structure in 3D (Fig. B8). If the companion is traveling through the x–z or y–z plane, a 2D cross-section through the wake of the companion in these planes is a 2D-circle-shape (see Figs B8 and B9), whose radius depends on the location of the slice relative to the wake. As the stellar pulsations meet the wake of the companion, strong shocks form in the x–z or y–z planes, which cluster to form arcs and bars. The multiple bars (top panel of Fig. B7) are mainly formed by the strong shocks between the upper and lower edges of the wake and the stellar pulsation; due to the proximity of the companion, the amplitude of the stellar pulsations is the highest when meeting the upper and lower edges of the wake. Fig. B8 represents a schematic illustration to illustrate the formation of the arcs/bars in the polar planes.

The bar-like structures can be seen in the y–z or x–z planes, only if the stellar pulsations meet the companion around z $\approx$0 or y $\approx$0, respectively. Otherwise, the structures will form at planes with z and y different from zero and slices through z = 0 and y = 0 do not show evident structures (e.g. model 21 in Figs B6 and B7). Therefore, the symmetry and the shape of these structures depend on the location of the cross-section slice and the orbital resonance.

3.5 Formation of a single spiral

If the companion is at a distance $d_{\rm comp} \gtrsim 4R_*$, the substellar companion creates a single spiral when traveling through the circumstellar medium of the AGB star. In Fig. 10 we show cross-section plots through the orbital plane for models 33, 36, 39, and 40, all showing a single spiral. Single spirals have been observed around several AGB stars (e.g. Mauron & Huggins 2006; Kim & Taam 2012a,b; Maercker et al. 2012; Decin et al. 2020; Homan et al. 2020; Randall et al. 2020). In these cases the system is composed of a binary system with a large orbital separation (several dozens of astronomical units). The formation of a single spiral in such binary systems is due to the reflex motion of the binary and the gravitational focusing of the mass lost from the giant star (e.g. Mastrodemos & Morris 1999;
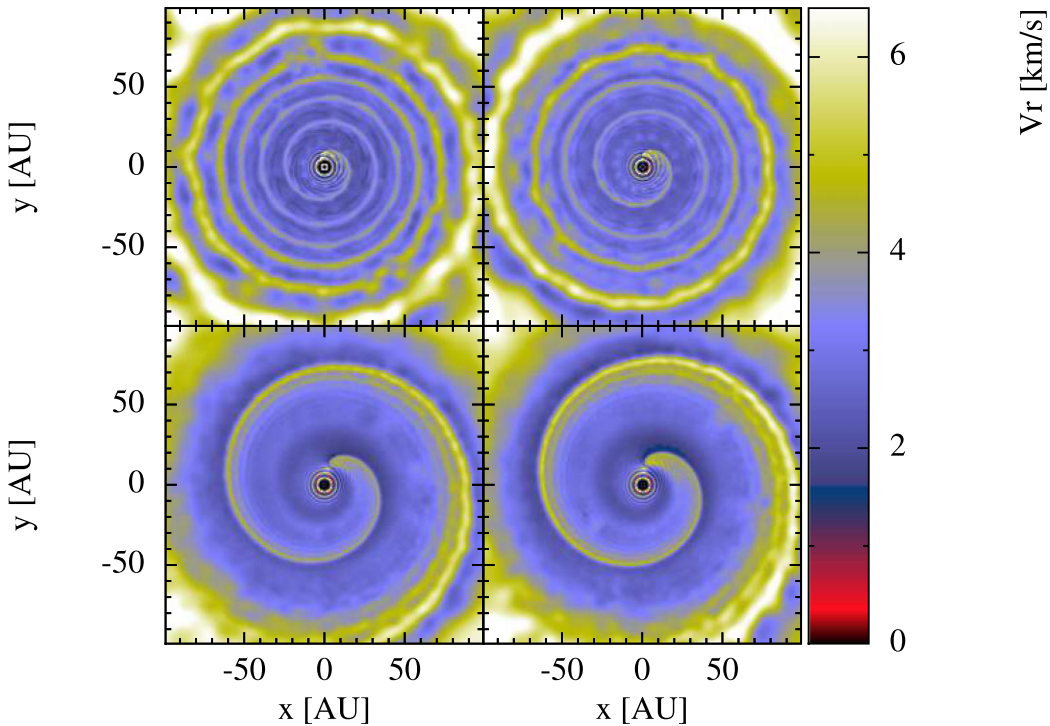
Figure 10. Top: 2D radial velocity cross-section through the orbital plane from models 33 (left-hand panel) and 36 (right-hand panel), after ≈ 76 pulsation cycles. Bottom: same for models 39 (left-hand panel) and 40 (right-hand panel), after ≈ 88 pulsation cycles. All models show a single spiral in the orbital plane.

Mohamed & Podsiadlowski 2007; Raga & Cantó 2008; Kim & Taam 2012b; Chen, Ivanova & Carroll-Nellenback 2020; Guerrero et al. 2020; Castellanos-Ramírez et al. 2021).

However, in the case of a substellar companion orbiting the AGB star at a moderate distance $d_{\mathrm{comp}} \sim 4 - 10 R_*$ and when $P_{\mathrm{orb}} \gg P_{\mathrm{puls}}$, the single spiral arm is formed due to the interaction of the wake of the companion with the circumstellar environment and the stellar pulsations. Due to the gravitational potential of the companion and its wider orbit, the companion drags a large number of particles behind it, increasing the density and velocity in the wake substantially. As the companion orbits the star and the gas moves outwards, the trailing wake of the companion forms a spiral structure centred at the companion. In addition, since P_{orb} is much larger than Ppuls, the companion meets a new cycle of shock waves after traveling a small fraction of its orbit. Each time the wake of the companion meets a new shock wave cycle, a shock is created. These shocks propagate in the radial direction and cluster into the spiral arm, enhancing its momentum. These shocks are imprinted on the spiral arm as enhanced velocity regions. In Fig. B10 we show a zoom-in plot on the shock formation regions for these four models, to highlight the interaction between the pulsations and the wake of the companion. The shocks can be seen on both the inner and leading arms of the spiral and they are more obvious on the inner one near the stellar pulsations, compared to the smoother leading arm. This is particularly the case for models 33 and 36 where the companion is closer to the star. In the case of simulations that assume continuous outflows with constant velocity winds (e.g. Kim & Taam 2012b), these shocks are not seen. For models 39 and 40, where the companion is at a distance of $10 R_*$, the spiral arms are smoother, however, the leading arm shows multiple components, forming discrete layers, due to the stellar pulsations. These discrete layers are formed by the gradient in velocity caused by the shock waves from the pulsations and are not typically seen in simulations with a constant velocity outflow.

For models with a single spiral arm (models 33 and 40), the spiral structures are well resolved in the density cross-sections (Fig. B1). Since in this case the spirals are created by the companion traveling through the circumstellar medium, the density in the wake of the companion is substantially larger compared to the surrounding medium. The single spiral structure (from model 40) is also clearly resolved in the entropy cross-section (Fig. B2).

The period of a single spiral arm, P_{sa}, is equal to P_{orb}. In this case, the spiral pattern repeats itself when the companion completes one full orbit. A time-evolution visualization of the models can be found in the supplementary material.

In Figs B11 and B12, we show cross-section plots of the same models in the polar, y–z and x–z planes, respectively. These plots slice vertically through the orbital plane and therefore instead of a single spiral arm we see multiple arcs on both sides of the star. The arcs in this case are slices through the spiral arm, showing its inner and leading arms. The number of arcs increases with increased winding of the spiral arm and the opening angle of the arcs is smaller for closer companions ($d_{\mathrm{comp}} \sim 4–5 R_*$, e.g, models 33 and 36) compared to more distance companions ($d_{\mathrm{comp}} \sim 10 R_*$, e.g. models 39 and 40). In all the models, the arcs are composed of multiple layers, which again are caused by the interaction of the wake with the stellar pulsations. The pulsations are clearly visible inside the first arc as spherical shock waves (see Fig. B10).

3.6 Testing different resolutions

We explore the effect of resolution on the outcome of our models. In Fig. 11 we show 2D radial velocity cross-section plots for four simulations with parameters similar to model 9 but for different resolutions: 2.5×10^5, 1.1×10^6, 4.2×10^6 (original model), and 8.5×10^6 particles. It is clear that the spirals are better resolved for higher number of particles. Increasing the number of particles in the simulation reduces the scale over which the particles' properties are
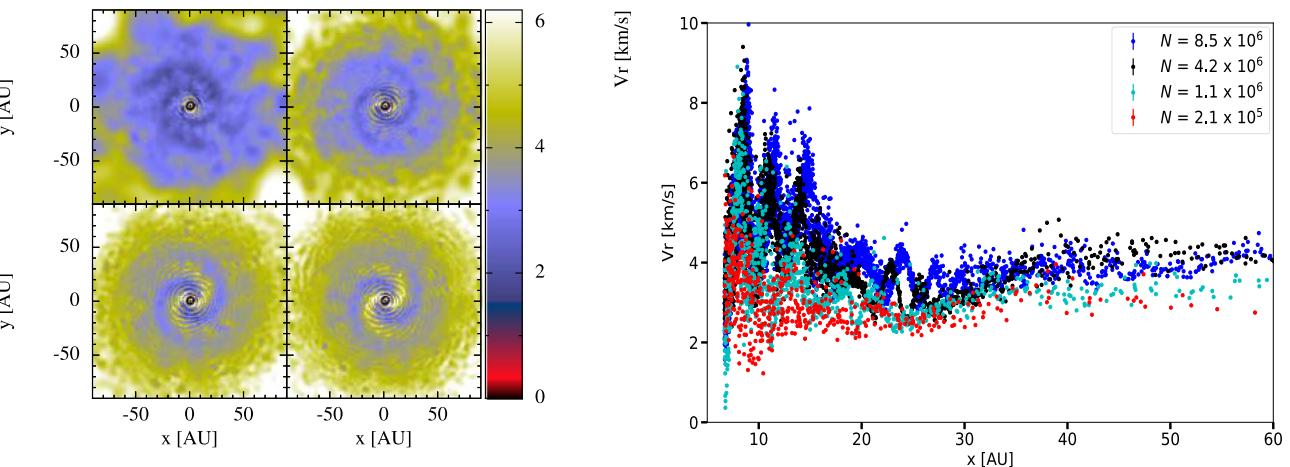
Figure 11. Left-hand panel: 2D radial velocity cross-section through the orbital plane for model 9 after 76 pulsation cycles, but using different resolutions. The models from left to right, top to bottom have the following number of particles: 2.1×10^5, 1.1×10^6, 4.2×10^6, and 8.5×10^6, respectively. The spirals are clearly better resolved when we increase the resolution of the simulation. Right-hand panel: radial velocity profiles of the same simulations, colour coded based on the resolution of the simulation as indicated in the legend.

smoothed, and therefore allows for better estimates of the properties of the particles at density and velocity discontinuities, such as the location of the shocks between the stellar pulsations and the wake of the companion. We also present radial velocity profiles for the four models in Fig. 11, showing a higher amplitude in the velocity of the gas at the shocks, which again implies that a higher resolution allows us to better determine the gas properties at shock discontinuities and to better resolve the spiral arms. Fig. B13 shows the density cross-section for the same models. The shocks are slightly better resolved for the simulations with higher resolution, yet the spiral structures are not evident, as discussed previously.

3.7 Including acceleration due to dust

We include acceleration due to dust in a few models to test its effect on the formation of spiral arms. For these models we use 1.1×10^6 particles for computational efficiency. We experiment with both silicate and carbonaceous dust, as detailed in Section 2.2.3. In Fig. 12 we present velocity cross-sections from four simulations. These simulations have the same parameters as models 9 and 39, but with acceleration from silicate-based and carbonaceous-based dust grains. In the simulations that have the same parameters as model 9, two spiral arms form. However, the spiral structures are noisier compared to the models that do not include dust. This is expected given the added dust acceleration. We also observe a single spiral arm in the models that have the same parameters as model 39. Again, the spiral structures are noisier due to the added dust acceleration. If we use higher resolution, e.g. 2.4×10^6 particles, similar to the rest of the models, we expect that the spiral structures will be better resolved (see Section 3.6). We discuss the effect of dust acceleration on the possibility of observing multiple spiral structures in Section 4.4.

4 DISCUSSION

4.1 The effect of the companion on the mass-loss

Our models show that the presence of a close-in companion around the pulsating star enhances the mass-loss. This is due to: (1) the gravitational pull exerted by the companion on the gas in the upper layers of the atmosphere and (2) the high-velocity and high-

temperature shocks between the wake of the companion and the stellar pulsation. These shocks lift material away from the star and enhance the outflow/mass-loss.

Since the gravitational potential of the companion is the main factor at play, there is a trend of higher mass-loss rate with increasing M_{comp} and decreasing d_{comp}. These trends are illustrated in Figs 13 and 14. The higher the M_{comp}, the greater the pull on the gas in the atmosphere and the stronger the shocks. The same effects manifest when the companion is closer to the star. While we show here the effect of one factor (presence of a companion) on the mass-loss rate, there are multiple factors that affect mass-loss in AGB stars, such as the pulsation mode, radiation pressure on dust, cooling, etc. (e.g. Höfner 2008; Wood 2015; McDonald & Zijlstra 2016; Höfner & Olofsson 2018; Groenewegen & Sloan 2018). In addition, changes in the atmosphere of the star caused by the nearby companion might lead to changes within the star's inner layers and eventually affect the mass-loss processes (e.g. Privitera et al. 2016a,b; Staff et al. 2016; Rao et al. 2018; Stephan et al. 2020; Rapoport, Bear & Soker 2021). Therefore, it is worth noting the limitations of our models in revealing any such effect on the stellar interior given that we only simulate the atmosphere and circumstellar environment of the star.

4.2 Effect of the companion mass and distance on the spiral arms

In models 9, 12, 13, 14, and 15 we study the effect of M_{comp} on the structure of the spiral arms and their contrast with the surrounding medium. For these models we adopt different companion masses (5, 10, 30, 40, and 50 M_{J}) for the same orbital period and orbital separation. In this case the orbital period and separation are intentionally fixed just to test the effect of different companion masses.

The models show that the velocity contrast of the spiral arms with the surrounding medium is higher for higher M_{comp} (see Fig. 15). The greater gravitational pull exerted by the heavier companion on the gas in the circumstellar environment and in the upper atmosphere of the star leads to stronger shocks of higher velocity and temperature. This is highlighted in Fig. 16 where we plot the radial velocity profiles from some of these models. The profiles show that the radial velocity contrast and the amplitude of the shocks is higher for higher M_{comp}. For model 11, the presence of a higher mass companion leads to an
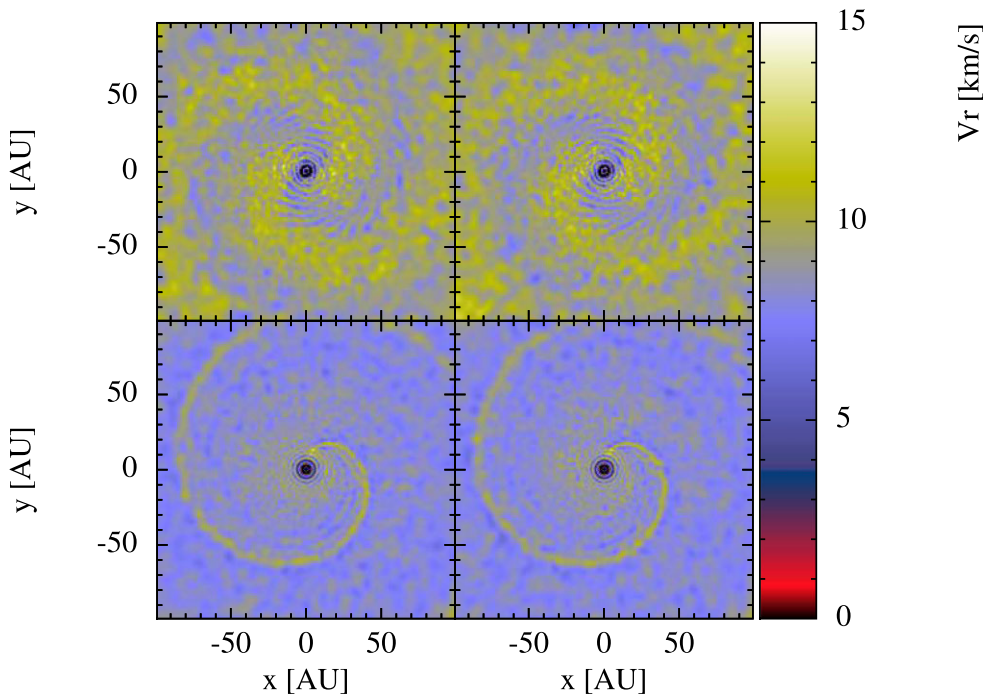
Figure 12. 2D radial velocity cross-section through the orbital plane for models 9 (top) and 39 (bottom), but this time including acceleration from silicate-based (left-hand panel) and amorphous carbon (right-hand panel) dust.
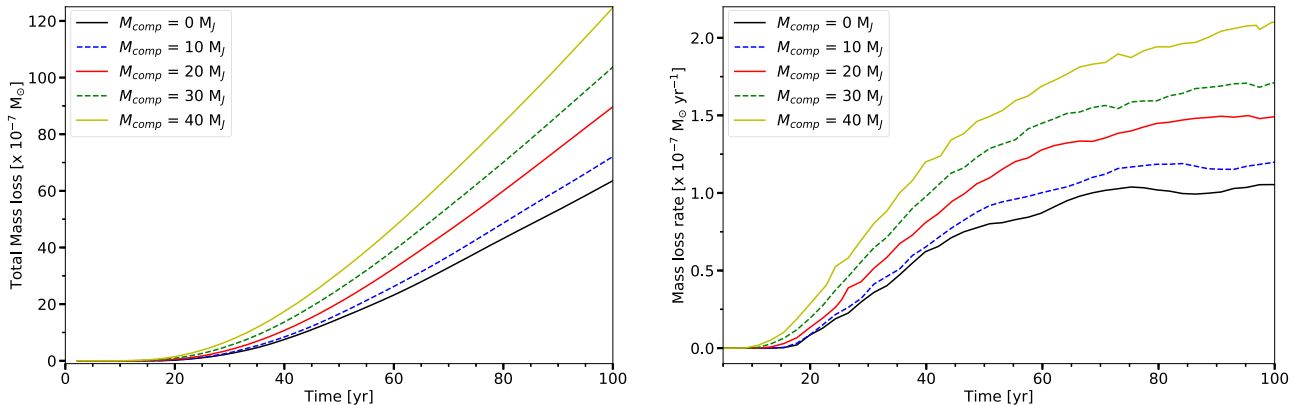

Figure 13. The evolution of the total mass-loss (left-hand panel) and the mass-loss rate (right-hand panel) per year per unit solar mass, for different $M_{\rm comp}$ at the same distance from the star. The models presented are model 0 (black solid line), model 13 (blue dashed line), model 14 (red solid line), model 9 (green dashed line), and model 15 (yellow solid line). The only parameter changed in these models is the companion mass. Both the total mass-loss and mass-loss rate increase with increasing $M_{\rm comp}$.

increase in the radial velocity of the gas by a factor of ≈ 2, compared to models 0 and 12 (Fig. 16).

In all the models presented in Fig. 15, two spiral arms form, with the exception of model 12 ($M_{\rm comp} = 5\,{\rm M_J}$). In this model, the gravitational pull exerted by the companion on the surrounding gas is relatively weak, leading to weak shocks and unresolved spiral arms. An increase in the resolution of the simulation might help resolve the spiral arms in such a case (see Section 3.6). Nevertheless, the 1D models of Wang & Willson (2012) show multiple spiral structures for a close-in companion with a mass = $5\,{\rm M_J}$. Similarly, a more distant companion with a mass = $5\,{\rm M_J}$ also gives rise to a single spiral structure in the grid-based models of Kim & Taam (2012b). This again emphasizes that the absence of spiral structures in our models for a companion mass $\lesssim 5\,{\rm M_J}$ is likely a numerical effect.

Our models also show that if the companion is closer to the star, the shocks between the companion's wake and the stellar pulsations are stronger – showing higher velocity and higher temperature. Fig. 17 represents the velocity profiles of model 2 and 21. For model 2 where the companion is closer to the star, the velocity contrast due to the shocks is higher compared to model 21.

4.3 Effect of the orbital period and resonance mode on the spiral arms

The $P_{\rm orb}$ and its resonance with $P_{\rm puls}$ plays the major role in determining the properties and morphology of the spiral arms (e.g. number, period, winding, etc). The higher the offset between $P_{\rm orb}/P_{\rm puls}$ and M/N, the shorter the period of the arms and vice versa. In Fig. 18,
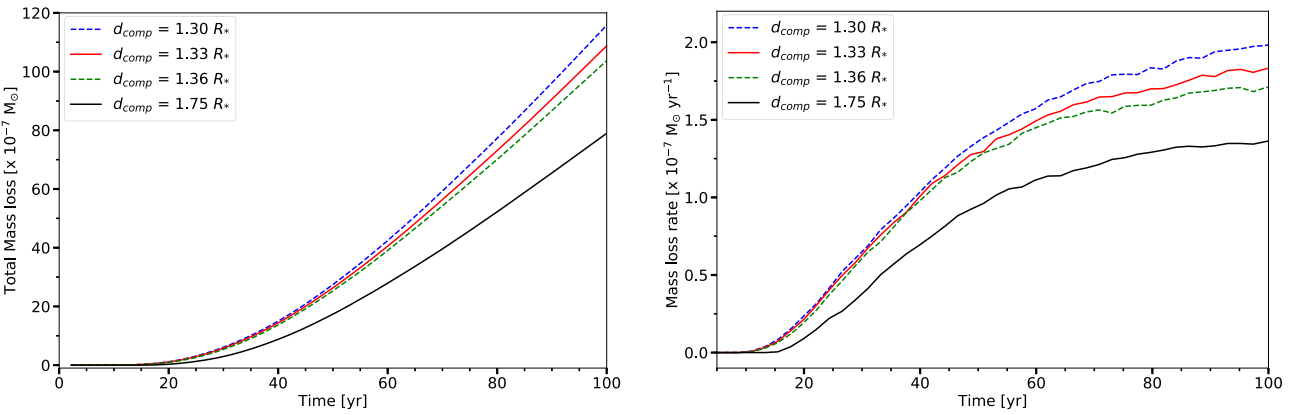
Figure 14. The evolution of the total mass-loss (left-hand panel) and the mass-loss rate (right-hand panel), per year per unit solar mass, for different d_{comp} with the same companion mass ($M_{comp} = 30\,M_J$). The models presented are model 1 (blue dashed line), model 4 (red solid line), model 9 (green dashed line), and model 20 (black solid line). The only parameter changed in these models is d_{comp}. Both the total mass-loss and mass-loss rate decrease with increasing d_{comp}.
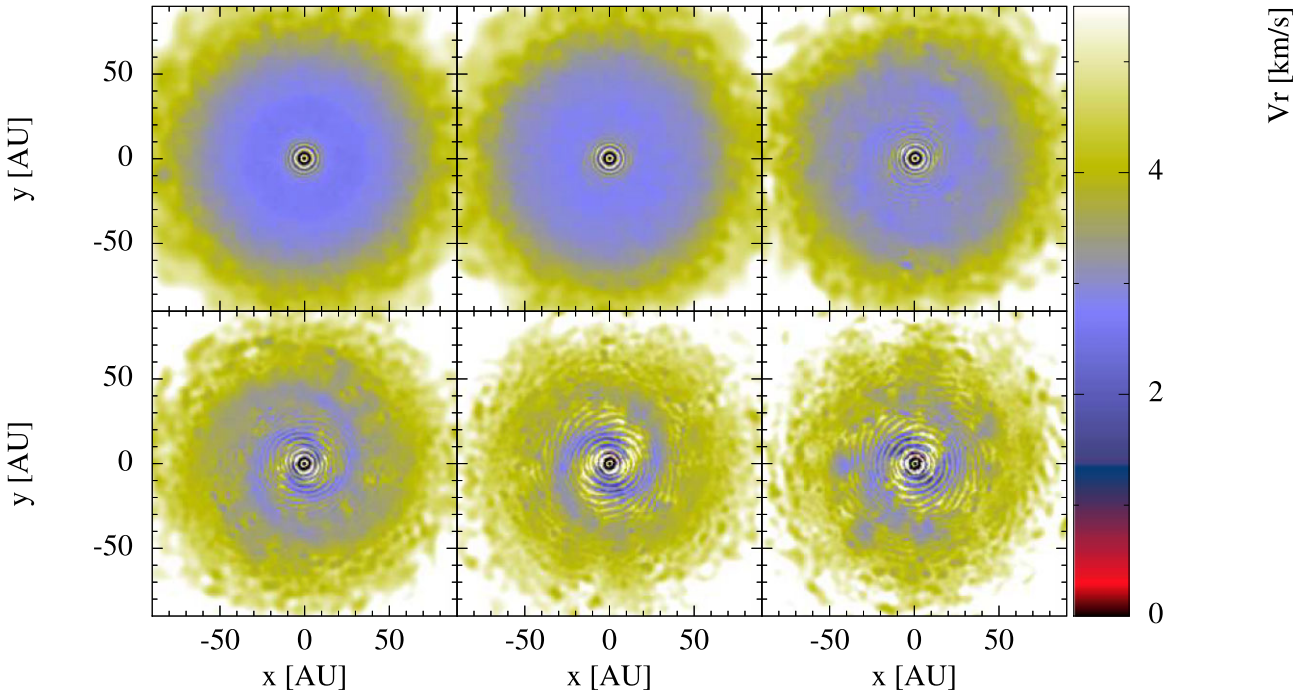
Figure 15. 2D radial velocity cross-section through the orbital plane from model 0 ($M_{comp} = 0$), 12 ($M_{comp} = 5\,M_J$), 13 ($M_{comp} = 10\,M_J$), 14 ($M_{comp} = 20\,M_J$), 9 ($M_{comp} = 30\,M_J$), and 40 ($M_{comp} = 50\,M_J$), going from left to right, top to bottom, after ~ 76 pulsation cycles. There is a trend of increasing velocity contrast between the spiral structures and their surrounding medium with increasing M_{comp}.

we highlight the effect of P_{orb} on the period of the spiral arms and their winding. At the same time-step of the simulation, the spirals experience different windings depending on the P_{orb} and therefore P_{sa}. Model 11 (with $P_{sa} = 7293$ d) shows more than one complete winding after ≈ 76 pulsation cycles, with a winding angle $\omega > 2\pi$ rad. However, for model 5 ($P_{sa} = 103885$ d) the winding angle $\omega < \pi/4$ rad after ≈ 76 pulsation cycles.

As seen pole-on from the z>0 direction, the spiral arms appear to rotate following a specific direction in the orbital plane. The direction of the apparent rotation depends on the ratio of P_{puls} to P_{orb}. If P_{puls}/P_{orb} is less than M/N, the apparent rotation of the spiral arms is in the counterclockwise direction, and if P_{puls}/P_{orb} is greater than M/N, then it is in the clockwise direction. Fig. B5 illustrates both cases, using models 2 and 6 as examples, showing the spiral arm locations

at different time-steps. In model 2 where $P_{puls}/P_{orb} = 0.508$, the spiral arms appear to rotate in the counterclockwise direction, however in model 6 where $P_{puls}/P_{orb} = 0.492$, the spiral arms appear to rotate in the clockwise direction. Nevertheless, the shocks that form the spiral arms are moving in the radial direction in both cases.

4.4 Can the spiral arms be observed?

The early (more than two decades ago) theoretical studies of single spirals forming in the outflows of evolved stars laid a solid foundation for further simulations and for our understanding and interpretation of the observations of such structures with current facilities. There are two main considerations in determining whether the multiple spirals simulated here will be observable: first, we need
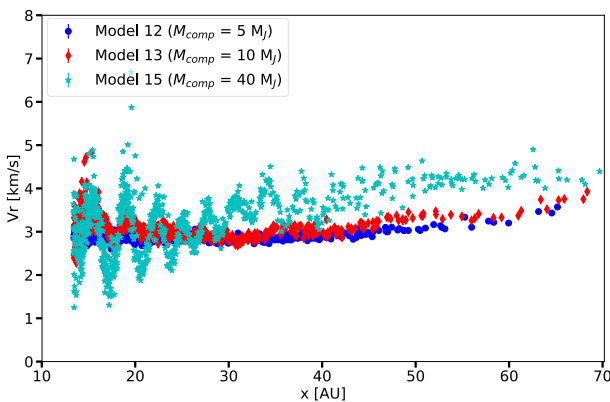
Figure 16. Radial velocity profiles along the x-axis from models 12 (blue circles), 13 (red diamonds), and 15 (cyan stars), after ≈ 76 pulsation cycles. The profiles show higher velocities for higher mass companion.
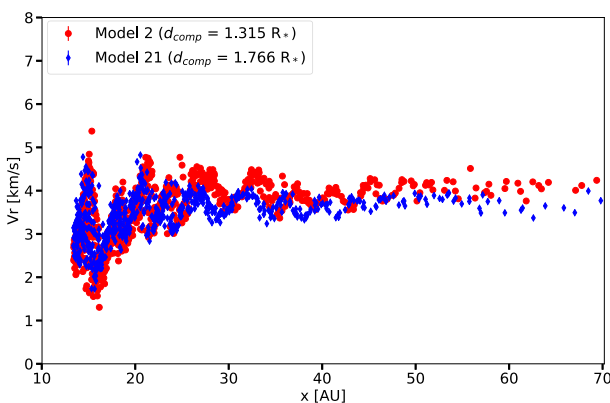

Figure 17. Radial velocity profiles along the x-axis from model 2 (red) and model 21 (blue) after ≈ 76 pulsation cycles. The shock velocities are slightly higher for model 2 where the companion is closer to the star's atmosphere.

to consider the companion survivability and the different factors that can affect the formation of evident spirals; second we need to consider the capabilities of current facilities/instruments to resolve such structures.

Several studies have been carried out to investigate the survival of planets around giant stars and their orbital evolution (e.g. Villaver & Livio 2007, 2009; Nordhaus et al. 2010; Kunitomo et al. 2011; Villaver et al. 2014). Nordhaus & Spiegel (2013) showed that most companions with orbits < 6 AU will be engulfed by stars with masses between 1 and 3 $M_\odot$. However, various parameters and mechanisms affect the survival of the planet (e.g. tidal drag, mass-loss, the system parameters), hence this topic is still an extensive field of research. Studying the survival of the companion and its orbital evolution are of course not the focus of this work. Our simulations assume that the companion is not engulfed by the star and therefore we exclude any decay in the orbit of the companion and we assume that the companion survives and is in a stable orbit over the simulation time-scale – all reasonable assumptions (Duncan & Lissauer 1998; Villaver & Livio 2007; Batygin & Laughlin 2008; Kervella et al. 2017; Vanderburg et al. 2020). However, if there is a change in the orbital period/separation (e.g. due to orbital decay), there would be implications for the possibility of observing the spiral structures: if the time-scale of the formation of the spirals is shorter than the time-scale of a stable orbit, it is likely that the spirals would not be observable. Whilst, if the time-scale of a stable orbit is longer than

the time-scale of the formation of spirals, such spirals could form and might last for a few thousands of years.

The presence of more than one substellar companion around the AGB star should lead to the interaction of both companions with the circumstellar environment and the stellar winds. This will likely cause even more complex structures, with the possibility of multiple, 'interfering' spiral arms, increasing the challenge to observe and distinguish the structures. The interaction of the stellar pulsations with multiple companions is not considered here, but will be the subject of our follow-up study.

Furthermore, our models are idealized – we assume a spherical, radially pulsating AGB star. While this assumption is reasonable, in reality the morphology of the atmosphere and the shock structures are much less spherically symmetric (Freytag et al. 2017). In a realistic outflow, we expect that the spiral arms might deviate from symmetric structures in the orbital plane and show more complexity, e.g. if the pulsations are more chaotic in a particular direction, it is possible that shocks cluster in a spiral arm only on one side of the orbital plane. This adds to the challenges of observing the spiral structures and determining the influence of a close-in companion on the circumstellar environment of the AGB star.

While the presence of acceleration due to dust can lead to less symmetric and noisier spiral structures, both Wang & Willson (2012)'s and our models show that despite the added acceleration due to radiation pressure on dust, observable spiral structures can form around the star. However, a more realistic formalism for dust acceleration is needed to better assess the formation of spiral arms in this case and the potential of observing them.

In several of our models, the spiral arms complete their first winding on a time-scale of 20 to 150 yr (e.g. models 1, 2, 6, 7, 8, 9, 10, 11; see Fig. 18). Therefore, we expect that in these cases the spiral arms will achieve several winding on a time-scale of the order of hundreds of years, which is short compared to an AGB star lifetime. This could make it difficult to distinguish and observe the spiral arms. However, in the case of P_{puls}/P_{orb} being very close to M/N (e.g. models 3, 4, and 5), the winding time-scale of the spiral arms jumps to a few thousand years, making it easier to observe and distinguish such multiple spiral arms. For Mira variables with pulsation periods of the order of a few thousand days, the formation and winding time-scales of the spiral arms become much longer (∼ thousands of years), increasing the chance of spotting multiple spiral arms in their circumstellar environments.

The inclination of the system also plays an important role in determining the observability of the structures, near-face-on spirals might be easier to detect compared to the arcs and bars that result looking edge-on at the orbital plane.

The multiple spiral structures in our models extend out to 70 AU, scales that are not far off for current and imminent high-resolution, high-sensitivity facilities. Facilities like ALMA which have revealed a diversity of structures around Galactic AGB stars (Lagadec & Chesneau 2015; Kervella et al. 2017; Brunner et al. 2019; Lagadec 2019; Homan et al. 2020), instruments with extreme adaptive optics such as SPHERE, intended to resolve the circumstellar environment of young stars and proto-planetary systems (Avenhaus et al. 2018; Sissa et al. 2018), and future instruments, such as the mid- and near-infrared cameras and imager on the *James Webb Space telescope* (Gardner et al. 2006) could offer us a chance to observe the multiple spiral structures. Given the difficulty to resolve the structures in density-space in our simulations, and that the outflows are cold and dusty, observations in velocity-space and at mm/submm and infrared wavelengths, stand the best chance of detecting the circumstellar features.
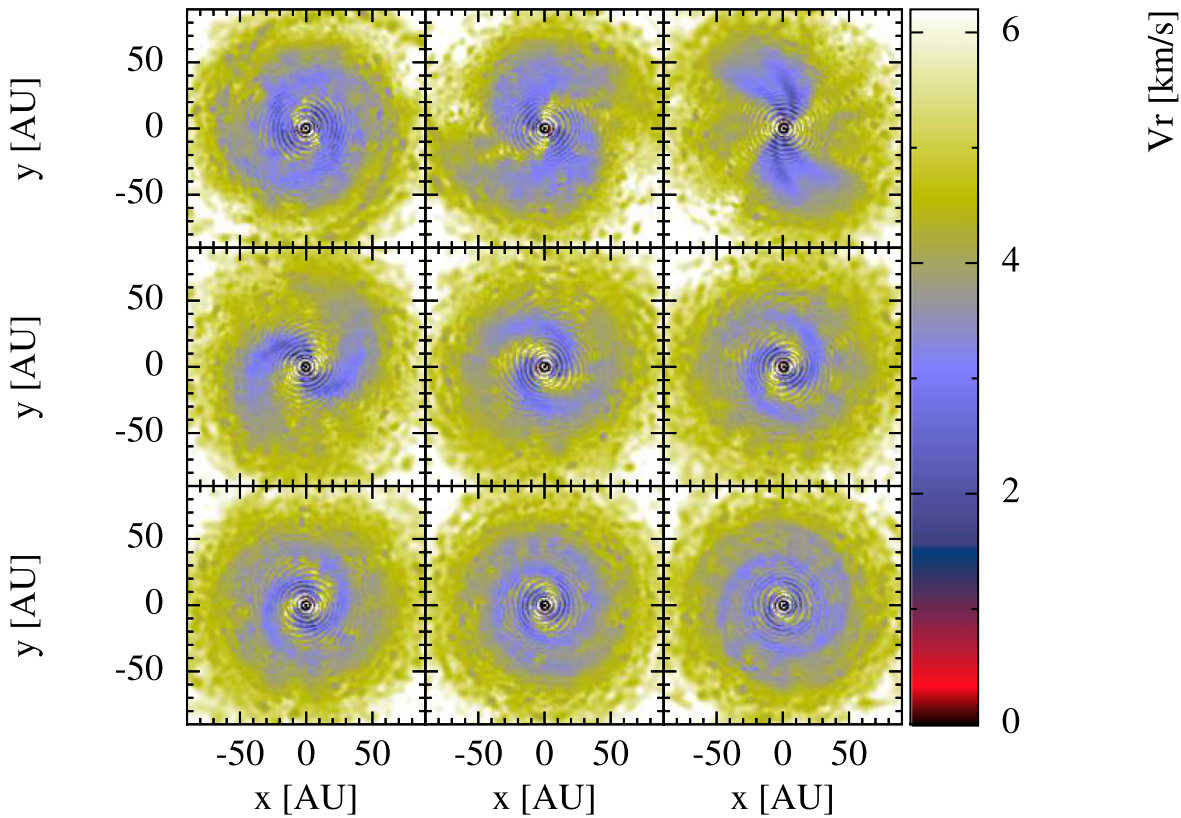
Figure 18. 2D radial velocity cross-section through the orbital plane from models 1 ($P_{orb} = 761$), 2 ($P_{orb} = 775$), 5 ($P_{orb} = 791$), 6 ($P_{orb} = 801$), 7 ($P_{orb} = 808$), 8 ($P_{orb} = 812$), 9 ($P_{orb} = 815$), 10 ($P_{orb} = 823$), and 11 ($P_{orb} = 833$), going from left to right, top to bottom, after ≈ 76 pulsation cycles. The models show the changing shape of the spiral structures with changing P_{orb}.

4.5 Implications for our future Solar system

Our Sun will evolve into an AGB star in around 5 billion years from now, pulsating with a period of the order of a year and with an outer stellar radius that could extend beyond Earth's orbit and as far as that of Mars (Iben & Renzini 1983). This process will likely be destructive for the inner planets and might affect the orbits of the gas-giants, particularly their semimajor axis and eccentricity (Debes & Sigurdsson 2002; Veras & Wyatt 2012). The orbit of the gas giants in our Solar system will possibly be stable for several billion years during the post-main sequence phase (e.g. Duncan & Lissauer 1998; Batygin & Laughlin 2008 and references therein). If the pulsation period of the Sun and the orbital period of, e.g. Jupiter achieve a certain resonance, the interaction between Jupiter and the solar pulsations might lead to the formation of multiple spiral structures, similar to the ones we obtained in our models. If Jupiter ends up in a much more extended orbit compared to the solar radius (Debes & Sigurdsson 2002), a single spiral arm could form due to the interaction of the wake of Jupiter with the circumsolar environment, similar to models 33 to 40.

In our simulations we did not resolve spiral structures for models with a companion mass $\lesssim 5\,M_J$. But a significant increase in the resolution of the simulations (e.g. an order of magnitude more particles) should allow us to resolve spiral structures for a companion mass of $1 - 5\,M_J$. However, we did not attempt this given the substantial increase in the computational time that might result from such increase in the resolution of the simulation. Nevertheless, the 1D models of Wang & Willson (2012) did result in the formation of multiple spiral arms for a companion mass of $5\,M_J$.

5 CONCLUSIONS AND SUMMARY

We have carried out 3D hydrodynamic models of mass-losing, pulsating AGB stars to simulate the effect of a close-in substellar companion on the morphology of the circumstellar environment of the star. Below is a summary of our results:

(i) If there is a resonance between the orbital period of the companion and the stellar pulsation, and if the companion is at a distance $d_{comp} < 3R_*$, the interaction between the wake of the companion and the stellar pulsations leads to the formation of strong shocks, which cluster in multiple spiral arms centred on the system. The number of the spiral arms is based on the resonance between the orbital and pulsation periods.

(ii) Similar to the models of Wang & Willson (2012), we found that the period of the spiral structure can be expressed as: $P_{sa} = \frac{P_{orb}P_{puls}}{|MP_{orb} - NP_{puls}|}$, where M and N represent the resonance mode M: N.

(iii) Our models demonstrate that the presence of a close-in companion enhances the mass-loss from the giant star.

(iv) Our 3D models show that complex structures such as bars- and arc-like structures form in the polar planes.

(v) If the companion is at a distance $d_{comp} > 4R_*$, the interaction between the companion and the stellar outflow leads to the formation of a single spiral arm.

(vi) We tested the effect of dust formation on the morphology of the outflow and we found that multiple or single spiral arms are still resolved when adding acceleration due to dust, but they are noisier.

(vii) Future high-resolution, high-sensitivity instruments might allow us to image these multiple spiral structures around AGB stars.

(viii) We also speculate that the interaction between Jupiter and the solar pulsations when our Sun turns into an AGB star might lead to the formation of spiral structures similar to those obtained in our simulations.

In this work, we make our first steps in investigating the effect of a substellar companion on the circumstellar environment of a pulsating AGB star in 3D. We plan to introduce more physically motivated mechanisms into our models, such as radiative cooling, radiative transfer, and different approaches to mimic a dust-driven wind. We also plan to study the effect of multiple substellar companions and planetary systems on the circumstellar environment of AGB stars.

ACKNOWLEDGEMENTS

DATA AVAILABILITY

The data are available upon request, particularly due to the large size of the output of the simulations (the size of each snapshot from the simulation is several 100s MB. The total size of one simulation is several GB).

REFERENCES

Abate C., Pols O. R., Izzard R. G., Mohamed S. S., de Mink S. E., 2013, A&A, 552, A26
Avenhaus H. et al., 2018, ApJ, 863, 44
Balick B., 1987, AJ, 94, 671
Balick B., Frank A., 2002, ARA&A, 40, 439
Balsara D. S., 1995, J. Comput. Phys., 121, 357
Barnes J., Hut P., 1986, Nature, 324, 446
Batygin K., Laughlin G., 2008, ApJ, 683, 1207
Beuzit J. L. et al., 2019, A&A, 631, A155
Bladh S., Höfner S., 2012, A&A, 546, A76
Bladh S., Höfner S., Nowotny W., Aringer B., Eriksson K., 2013, A&A, 553, A20
Bowen G. H., 1988, ApJ, 329, 299
Brucalassi A. et al., 2014, A&A, 561, L9
Brunner M., Mecina M., Maercker M., Dorfi E. A., Kerschbaum F., Olofsson H., Rau G., 2019, A&A, 621, A50
Castellanos-Ramírez A., Rodríguez-González A., Meliani Z., Rivera-Ortiz P. R., Raga A. C., Cantó J., 2021, MNRAS, 507, 4044
Chen Z., Frank A., Blackman E. G., Nordhaus J., Carroll-Nellenback J., 2017, MNRAS, 468, 4465
Chen Z., Ivanova N., Carroll-Nellenback J., 2020, ApJ, 892, 110
Cherchneff I., 2006, A&A, 456, 1001
Corradi R. L. M., Schönberner D., Steffen M., Perinotto M., 2000, A&A, 354, 1071
Corradi R. L. M., Sánchez-Blázquez P., Mellema G., Gianmanco C., Schwarz H. E., 2004, A&A, 417, 637

Corradi R. L. M. et al., 2011, MNRAS, 410, 1349
Debes J. H., Sigurdsson S., 2002, ApJ, 572, 556
Decin L., Richards A. M. S., Neufeld D., Steffen W., Melnick G., Lombaert R., 2015, A&A, 574, A5
Decin L. et al., 2020, Science, 369, 1497
Doan L. et al., 2017, A&A, 605, A28
Doan L. et al., 2020, A&A, 633, A13
Döllinger M. P., Hartmann M., 2021, ApJS, 256, 10
Duncan M. J., Lissauer J. J., 1998, Icarus, 134, 303
Eriksson K., Nowotny W., Höfner S., Aringer B., Wachter A., 2014, A&A, 566, A95
Feast M. W., Glass I. S., Whitelock P. A., Catchpole R. M., 1989, MNRAS, 241, 375
Freytag B., Höfner S., 2008, A&A, 483, 571
Freytag B., Liljegren S., Höfner S., 2017, A&A, 600, A137
Gail H.-P., Sedlmayr E., 1988, A&A, 206, 153
Gardner J. P. et al., 2006, Space Sci. Rev., 123, 485
Gauger A., Sedlmayr E., Gail H.-P., 1990, A&A, 235, 345
Gawryszczak A. J., Mikołajewska J., Różyczka M., 2002, A&A, 385, 205
Gettel S., Wolszczan A., Niedzielski A., Nowak G., Adamów M., Zieliński P., Maciejewski G., 2012a, ApJ, 756, 53
Gettel S., Wolszczan A., Niedzielski A., Nowak G., Adamów M., Zieliński P., Maciejewski G., 2012b, ApJ, 745, 28
Gilman R. C., 1972, ApJ, 178, 423
Gingold R. A., Monaghan J. J., 1977, MNRAS, 181, 375
Groenewegen M. A. T., Sloan G. C., 2018, A&A, 609, A114
Guerrero M. A., Ramos-Larios G., Toalá J. A., Balick B., Sabin L., 2020, MNRAS, 495, 2234
Höfner S., 2008, A&A, 491, L1
Höfner S., Olofsson H., 2018, A&AR, 26, 1
Höfner S., Bladh S., Aringer B., Eriksson K., 2022, A&A, 657, A109
Homan W., Cannon E., Montargès M., Richards A. M. S., Millar T. J., Decin L., 2020, A&A, 642, A93
Iben I. J., Renzini A., 1983, ARA&A, 21, 271
Jeong G., Lee B. C., Park M. G., Bang T. Y., Han I., 2021, preprint (arXiv:2111.08899)
Kahn F. D., Breitschwerdt D., 1990, MNRAS, 242, 505
Kervella P. et al., 2017, The Messenger, 167, 20
Khouri T., Vlemmings W. H. T., Olofsson H., Ginski C., De Beck E., Maercker M., Ramstedt S., 2018, A&A, 620, A75
Kim H., Taam R. E., 2012a, ApJ, 759, L22
Kim H., Taam R. E., 2012b, ApJ, 744, 136
Kim H. et al., 2015, ApJ, 814, 61
Kunitomo M., Ikoma M., Sato B., Katsuta Y., Ida S., 2011, ApJ, 737, 66
Lagadec E., 2018, Galaxies, 6, 99
Lagadec E., 2019, in Kerschbaum F., Groenewegen M., Olofsson H., eds, Proc. IAU Symp. 343, Why Galaxies Care about AGB Stars: A Continuing Challenge through Cosmic Time. Cambridge Univ. Press, Cambridge, p. 141
Lagadec E., Chesneau O., 2015, in Kerschbaum F., Wing R. F., Hron J., eds, ASP Conf. Ser. Vol. 497, Why Galaxies Care about AGB Stars III: A Closer Look in Space and Time. Astron. Soc. Pac., San Francisco, p. 145
Lagadec E. et al., 2011a, MNRAS, 417, 32
Lagadec E., Zijlstra A. A., Oudmaijer R. D., Verhoelst T., Cox N. L. J., Szczerba R., Mékarnia D., van Winckel H., 2011b, A&A, 534, L10
Lamers H. J. G. L. M., Cassinelli J. P., 1999, Introduction to Stellar Winds. Cambridge Univ. Press, Cambridge, p. 452
Liu Y.-J. et al., 2008, ApJ, 672, 553
Lucy L. B., 1977, AJ, 82, 1013
Lykou F., Chesneau O., Zijlstra A. A., Castro-Carrizo A., Lagadec E., Balick B., Smith N., 2011, A&A, 527, A105
McDonald I., Zijlstra A. A., 2016, ApJ, 823, L38
Maercker M. et al., 2012, Nature, 490, 232
Maes S., Homan W., Malfait J., Siess L., Bolte J., De Ceuster F., Decin L., 2021, A&A, 653, A25
Malfait J., Homan W., Maes S., Bolte J., Siess L., De Ceuster F., Decin L., 2021, A&A, 652, A51
Manick R., Miszalski B., McBride V., 2015, MNRAS, 448, 1789

Marshall J. P., Wittenmyer R. A., Horner J., Clark J., Mengel M. W., Hinse T. C., Agnew M. T., Kane S. R., 2019, AJ, 157, 1

Mastrodemos N., Morris M., 1999, ApJ, 523, 357

Mattsson L., Wahlin R., Höfner S., 2010, A&A, 509, A14

Mauron N., Huggins P. J., 2006, A&A, 452, 257

Mohamed S., Podsiadlowski P., 2007, in Napiwotzki R., Burleigh M. R., eds, ASP Conf. Ser. Vol. 372, 15th European Workshop on White Dwarfs. Astron. Soc. Pac., San Francisco, p. 397

Mohamed S., Podsiadlowski P., 2012, Balt. Astron., 21, 88

Monaghan J. J., 1992, ARA&A, 30, 543

Monaghan J. J., Gingold R. A., 1983, J. Comput. Phys., 52, 374

Montez, Rodolfo J., Ramstedt S., Kastner J. H., Vlemmings W., Sanchez E., 2017, ApJ, 841, 33

Morris M., Sahai R., Matthews K., Cheng J., Lu J., Claussen M., Sánchez-Contreras C., 2006, in Barlow M. J., Méndez R. H., eds, Proc. IAU Symp. 234, Planetary Nebulae in our Galaxy and Beyond. Cambridge Univ. Press, Cambridge, p. 469

Myasnikov A. V., Belov N. A., Gustafsson B., Eriksson K., 2000, Ap&SS, 274, 231

Niedzielski A. et al., 2007, ApJ, 669, 1354

Niedzielski A., Goździewski K., Wolszczan A., Konacki M., Nowak G., Zieliński P., 2009a, ApJ, 693, 276

Niedzielski A., Nowak G., Adamów M., Wolszczan A., 2009b, ApJ, 707, 768

Niedzielski A., Wolszczan A., Nowak G., Adamów M., Kowalik K., Maciejewski G., Deka-Szymankiewicz B., Adamczyk M., 2015, ApJ, 803, 1

Nordhaus J., Blackman E. G., 2006, MNRAS, 370, 2004

Nordhaus J., Spiegel D. S., 2013, MNRAS, 432, 500

Nordhaus J., Spiegel D. S., Ibgui L., Goodman J., Burrows A., 2010, MNRAS, 408, 631

Nowak G., Niedzielski A., Wolszczan A., Adamów M., Maciejewski G., 2013, ApJ, 770, 53

Nowotny W., Aringer B., Höfner S., Eriksson K., 2013, A&A, 552, A20

Olofsson H., Maercker M., Eriksson K., Gustafsson B., Schöier F., 2010, A&A, 515, A27

Ostlie D. A., Cox A. N., 1986, ApJ, 311, 864

Price D. J., 2007, Publ. Astron. Soc. Aust., 24, 159

Privitera G., Meynet G., Eggenberger P., Vidotto A. A., Villaver E., Bianda M., 2016a, A&A, 591, A45

Privitera G., Meynet G., Eggenberger P., Vidotto A. A., Villaver E., Bianda M., 2016b, A&A, 593, A128

Quirrenbach A., Trifonov T., Lee M. H., Reffert S., 2019, A&A, 624, A18

Raga A. C., Cantó J., 2008, ApJ, 685, L141

Ramstedt S. et al., 2014, A&A, 570, L14

Ramstedt S. et al., 2017, A&A, 605, A126

Ramstedt S. et al., 2020, A&A, 640, A133

Randall S. K., Trejo A., Humphreys E. M. L., Kim H., Wittkowski M., Boboltz D., Ramstedt S., 2020, A&A, 636, A123

Rao S., Meynet G., Eggenberger P., Haemmerlé L., Privitera G., Georgy C., Ekström S., Mordasini C., 2018, A&A, 618, A18

Rapoport I., Bear E., Soker N., 2021, MNRAS, 506, 468

Sabin L., Zijlstra A. A., Greaves J. S., 2007, MNRAS, 376, 378

Saladino M. I., Pols O. R., 2019, A&A, 629, A103

Saladino M. I., Pols O. R., Abate C., 2019, A&A, 626, A68

Sato B. et al., 2003, ApJ, 597, L157

Sato B. et al., 2007, ApJ, 661, 527

Sato B. et al., 2008, PASJ, 60, 539

Schoenberner D., 1981, A&A, 103, 119

Schönberner D., Jacob R., Steffen M., Perinotto M., Corradi R. L. M., Acker A., 2005, A&A, 431, 963

Simis Y. J. W., Icke V., Dominik C., 2001, A&A, 371, 205

Sissa E. et al., 2018, A&A, 613, L6

Soker N., 1998, ApJ, 496, 833

Soszyński I. et al., 2021, ApJ, 911, L22

Springel V., 2005, MNRAS, 364, 1105

Springel V., Hernquist L., 2002, MNRAS, 333, 649

Staff J. E., De Marco O., Macdonald D., Galaviz P., Passy J.-C., Iaconi R., Low M.-M. M., 2016, MNRAS, 455, 3511

Starkenburg E., Shetrone M. D., McConnachie A. W., Venn K. A., 2014, MNRAS, 441, 1217

Steffen M., Szczerba R., Schoenberner D., 1998, A&A, 337, 149

Stephan A. P., Naoz S., Gaudi B. S., Salas J. M., 2020, ApJ, 889, 45

Struck C., Cohanim B. E., Willson L. A., 2002, ApJ, 572, L83

Theuns T., Boffin H. M. J., Jorissen A., 1996, MNRAS, 280, 1264

Trabucchi M., Mowlavi N., Lebzelter T., 2021, A&A, 656, A66

Ueta T. et al., 2014, A&A, 565, A36

van Winckel H., 2003, ARA&A, 41, 391

Vanderburg A. et al., 2020, Nature, 585, 363

Veras D., Wyatt M. C., 2012, MNRAS, 421, 2969

Villaver E., Livio M., 2007, ApJ, 661, 1192

Villaver E., Livio M., 2009, ApJ, 705, L81

Villaver E., Livio M., Mustill A. J., Siess L., 2014, ApJ, 794, 3

Wang Q., Willson L. A., 2012, ApJ, 755, 136

Whitelock P. A., Feast M. W., van Leeuwen F., 2008, MNRAS, 386, 313

Wood P. R., 1979, ApJ, 227, 220

Wood P. R., 2015, MNRAS, 448, 3829

Wootten A., Thompson A. R., 2009, IEEE Proc., 97, 1463

SUPPORTING INFORMATION

Supplementary data are available at *MNRAS* online.

model_6_paper.mp4
model_9_paper.mp4
model_21_paper.mp4
model_26_paper.mp4
model_33_paper.mp4
model_39_paper.mp4
multi_spirals_final.mp4

Please note: Oxford University Press is not responsible for the content or functionality of any supporting materials supplied by the authors. Any queries (other than missing material) should be directed to the corresponding author for the article.

APPENDIX A: COMPANION PROPERTIES

For a circular orbit with $M_{\rm comp} << M_*$, the constant relative velocity is given by:

$$v_{\rm comp} = (GM_*/d_{\rm comp})^{\frac{1}{2}}, \tag{A1}$$

where G is the gravitational constant, M_* is the mass of the star, and $d_{\rm comp}$ is the orbital radius of the companion. The angular momentum of an object is in general given by $\vec{L} = \vec{r} \times \vec{p}$, where $\vec{r}$ is the vector from the centre of rotation and $\vec{p}$ is the linear momentum. For a circular orbit, the position vector is always tangential to the orbit, thus, the angular momentum can be written as $L = rp = rmv$. The angular momentum of the companion can then be derived using: $L = m(GM_*d_{\rm comp})^{\frac{1}{2}}$. We can write then:

$$d_{\rm comp} = \frac{L^2}{M_{\rm comp}^2 GM_*} \tag{A2}$$

From Kepler's third law we can write:

$$L^3 = \frac{P_{\rm orb}G^2M_{\rm comp}^3M_*^2}{2\pi} \tag{A3}$$

Using equations (A2) and (A3) we can then derive $d_{\rm comp}$ for every $P_{\rm orb}$ and vice versa. The model parameters along with the companion properties are stored in Table A1.

Table A1. Models parameters.

Model	M_{comp} (M$_J$)	d_{comp} (R_*)	P_{orb} (d)	P_{puls}/P_{orb}	$M{:}N$	N_{sa}	P_{sa} (d)	U_{amp} (km s^{-1})
1	30	1.299	761	0.517	1:2	2	11 105	4.0
2	30	1.315	775	0.508	1:2	2	23 488	4.0
3	30	1.326	785	0.501	1:2	2	103 097	4.0
4	30	1.330	788	0.500	1:2	2	–	4.0
5	30	1.333	791	0.498	1:2	2	103 885	4.0
6	30	1.344	801	0.492	1:2	2	24 276	4.0
7	30	1.352	808	0.487	1:2	2	15 918	4.0
8	30	1.356	812	0.485	1:2	2	13 330	4.0
9	30	1.360	815	0.483	1:2	2	11 893	4.0
10	30	1.369	823	0.478	1:2	2	9265	4.0
11	30	1.380	833	0.472	1:2	2	7293	4.0
12	5	1.360	815	0.483	1:2	2	11 893	4.0
13	10	1.360	815	0.483	1:2	2	11 893	4.0
14	20	1.360	815	0.483	1:2	2	11 893	4.0
15	40	1.360	815	0.483	1:2	2	11 893	4.0
16	20	1.091	586	0.672	2:3	3	23 088	4.0
17	20	1.104	596	0.661	2:3	3	23 482	4.0
18	30	1.721	1160	0.339	1:3	3	20 775	4.0
19	30	1.731	1170	0.336	1:3	3	38 415	4.0
20	30	1.754	1194	0.329	1:3	3	39 203	4.0
21	30	1.766	1204	0.326	1:3	3	21 563	4.0
22	40	1.766	1204	0.326	1:3	3	21 563	4.0
23	20	1.010	522	0.754	3:4	4	20 567	4.0
24	20	1.019	529	0.744	3:4	4	18 948	4.0
25	30	1.019	529	0.744	3:4	4	18 948	4.0
26	50	2.093	1556	0.253	1:4	4	30 653	4.0
27	40	2.100	1564	0.251	1:4	4	51 351	4.0
28	40	2.122	1588	0.248	1:4	4	52 139	4.0
29	50	2.129	1596	0.246	1:4	4	31 441	4.0
30	50	2.138	1606	0.245	1:4	4	21 092	4.0
31	30	1.360	815	0.483	1:2	2	11 893	5.0
32	30	1.360	815	0.483	1:2	2	11 893	6.0
33	40	4.0	4033	0.069	–	1	4033	4.0
34	50	4.0	4015	0.069	–	1	4015	4.0
35	40	5.0	5637	0.069	–	1	5637	4.0
36	50	5.0	5611	0.069	–	1	5611	4.0
37	40	10.0	15 943	0.069	–	1	15 943	4.0
38	50	10.0	15 870	0.069	–	1	15 870	4.0
39	80	10.0	15 658	0.069	–	1	15 658	4.0
40	100	10.0	15 521	0.069	–	1	15 521	4.0

APPENDIX B: COMPLEMENTARY PLOTS

In this appendix we present complementary plots.
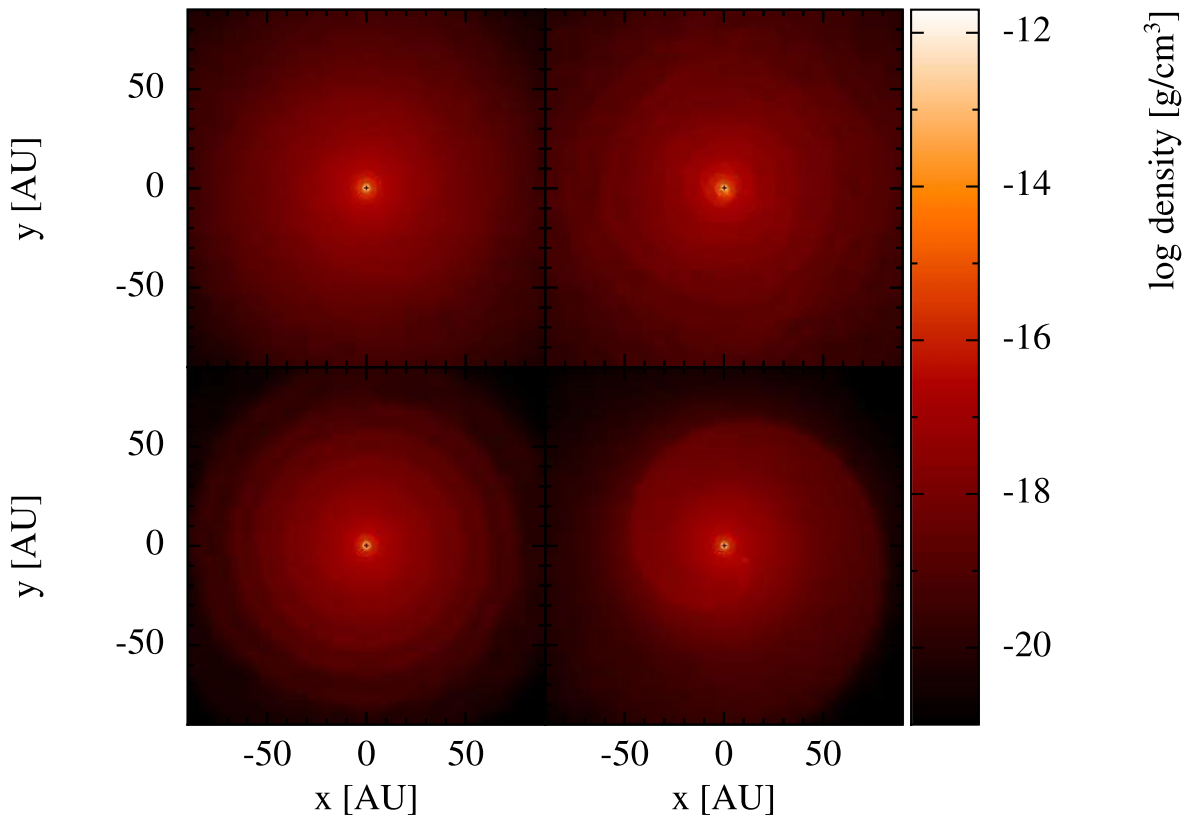
Figure B1. 2D density cross-section slices through the orbital plane after $\simeq 76$ pulsation cycle for model 9 (top left), model 26 (top right), model 33 (bottom left), and model 40 (bottom right). In models where multiple spiral arms form (top panels), the spiral structures are not well resolved in the density plots. However, in models where a single spiral arm forms (bottom panels), the spiral structures are well resolved in the density plots.
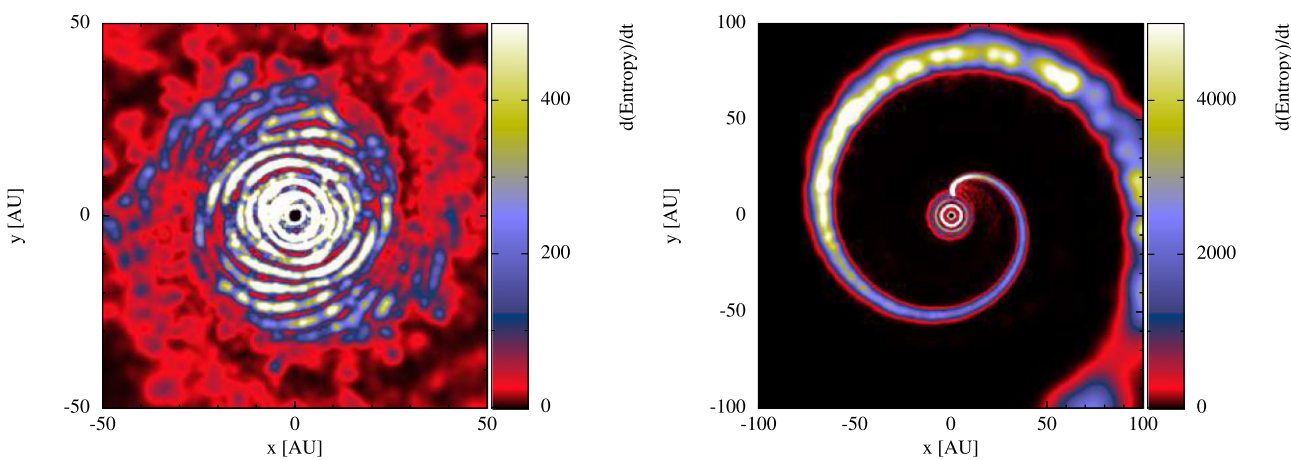
Figure B2. 2D entropy cross-section plots from models 9 (left-hand panel) and 40 (right-hand panel), after ≈ 76 and ≈ 89 pulsation cycles, respectively.
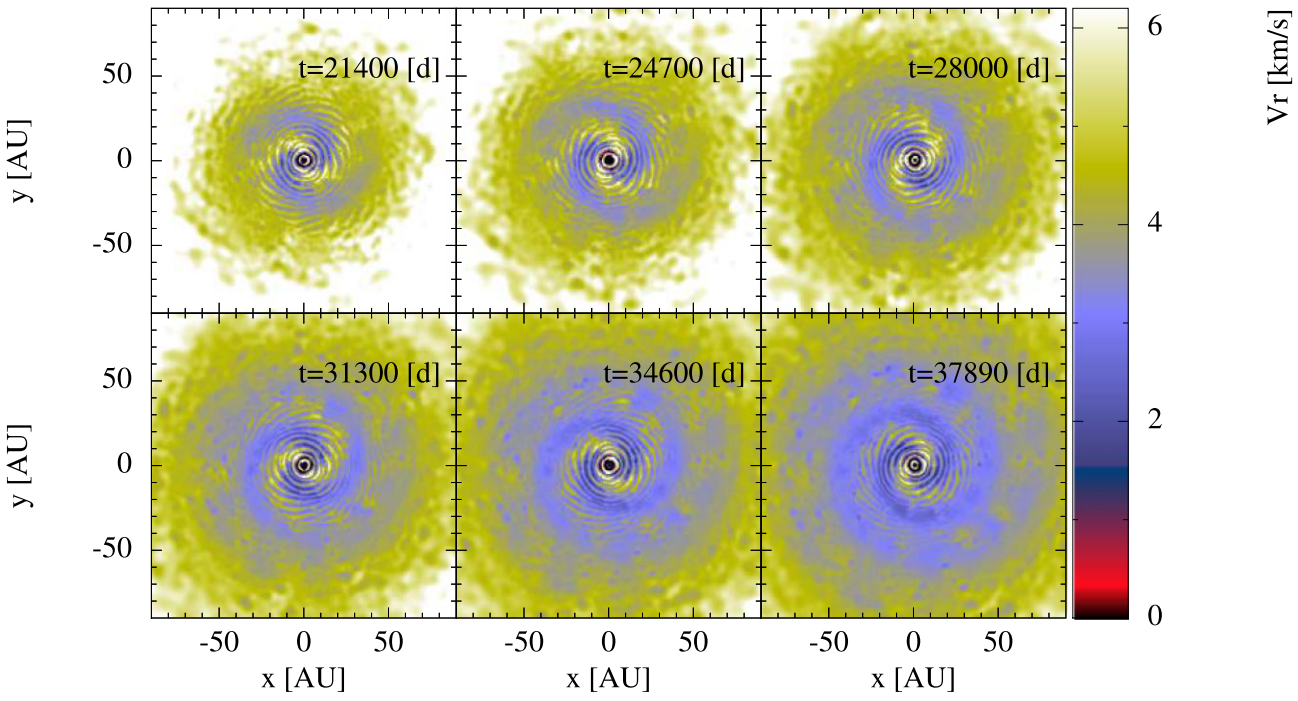
Figure B3. 2D radial velocity cross-section slices through the orbital plane from model 9 at different time-steps, in ascending order from left to right, top to bottom, showing the winding of the spiral arms as a function of time. t is the time in days elapsed since the start of the simulation.
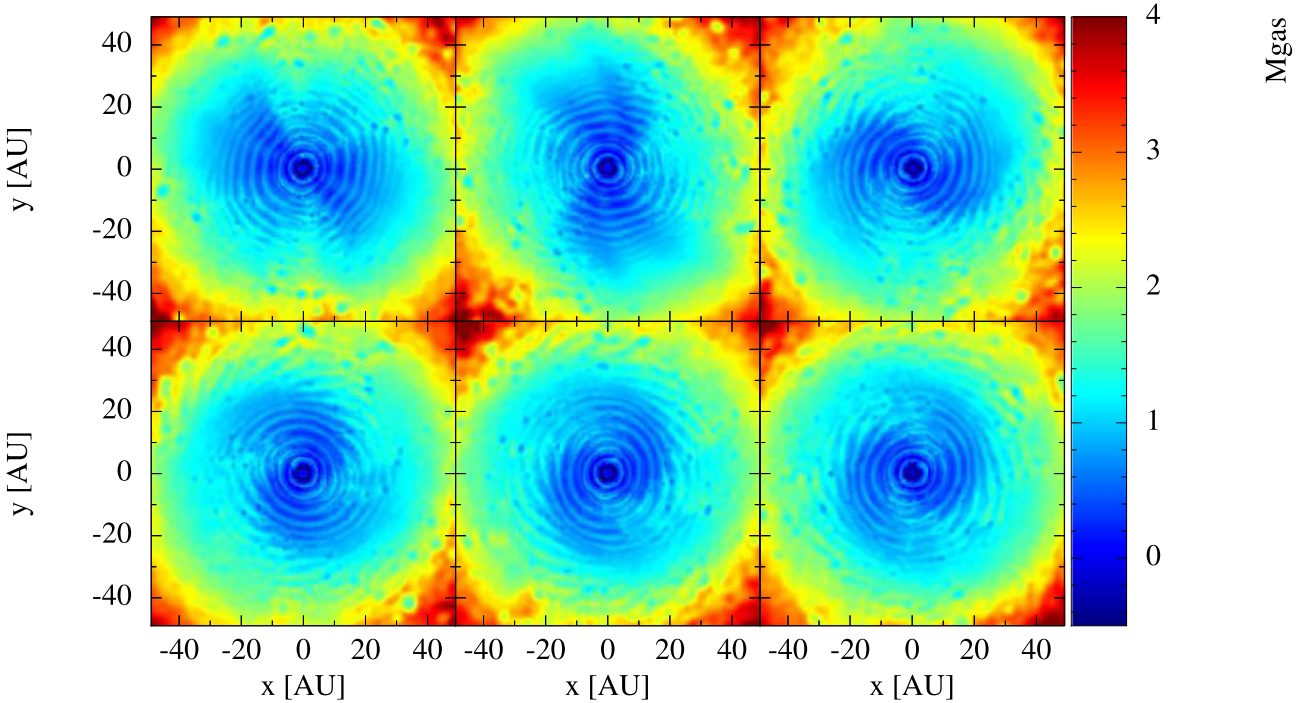
Figure B4. 2D M_{gas} cross-section slices through the orbital plane after ≈ 76 pulsation cycles for models 4, 5, 6, 7, 8, and 9, going from left to right, top to bottom. The spiral arms are propagating in the radial direction close to a supersonic speed ($M_{\mathrm{sa}} \gtrsim 1$) in most of the models.
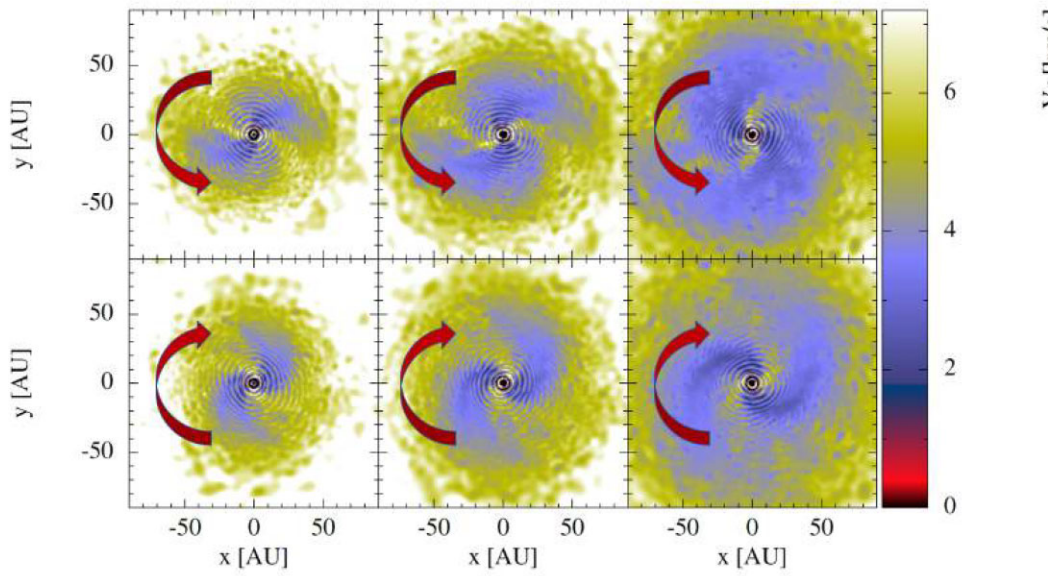
Figure B5. 2D radial velocity cross-section through the orbital plane from models 2 (top) and 6 (bottom) after 46, 59, and 80 pulsation cycles, from left to right. The red arrows indicate the apparent direction of rotation of the spiral arms. In model 2 the spiral arms are rotating in the counter-clockwise direction, however in model 6 the spiral arms are rotating in the clockwise direction.
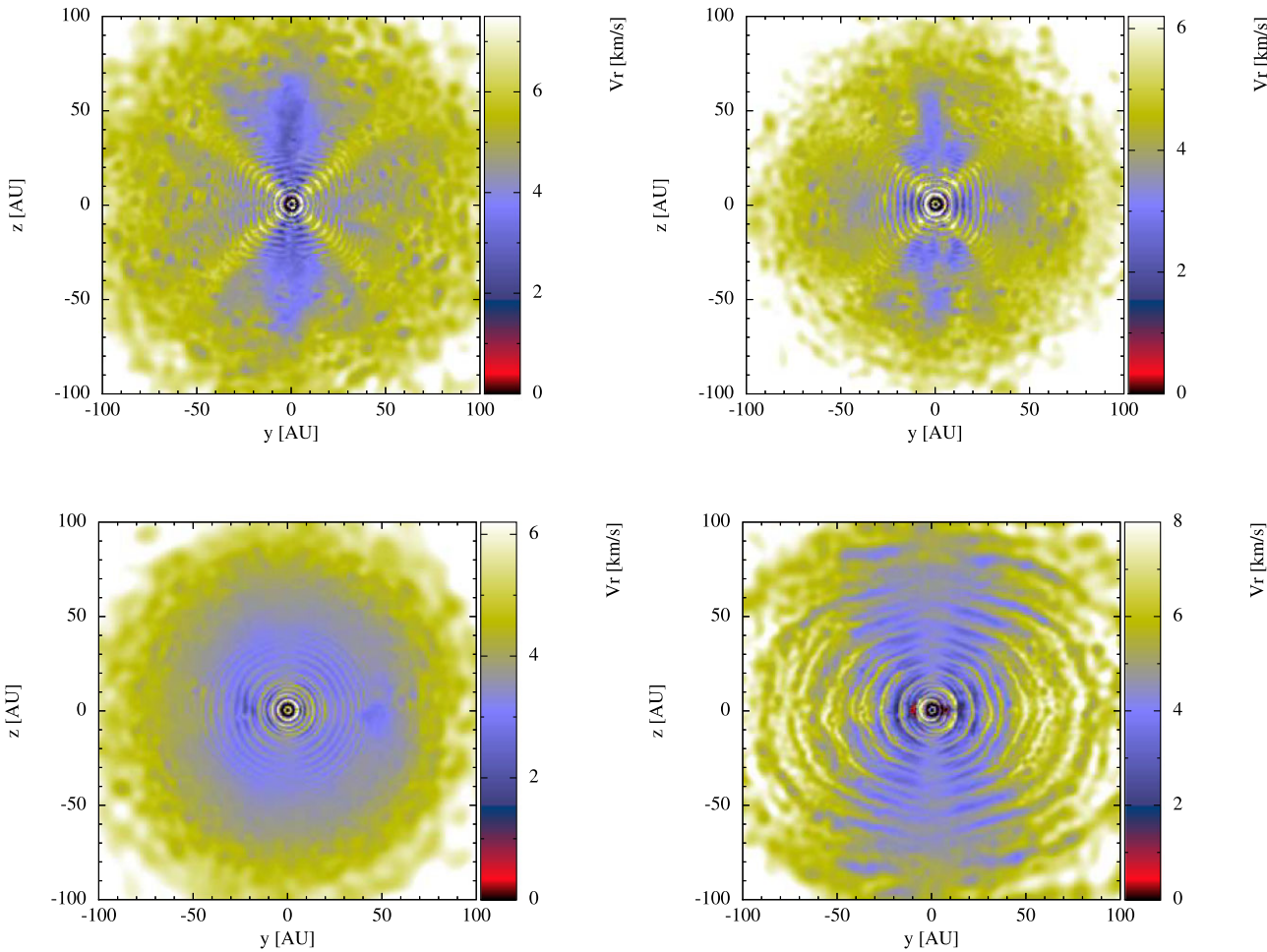
Figure B6. 2D velocity cross-section slices through the y–z plane after ~ 76 pulsation cycle for models 4 (top left), 9 (top right), 21 (bottom left), and 26 (bottom right).
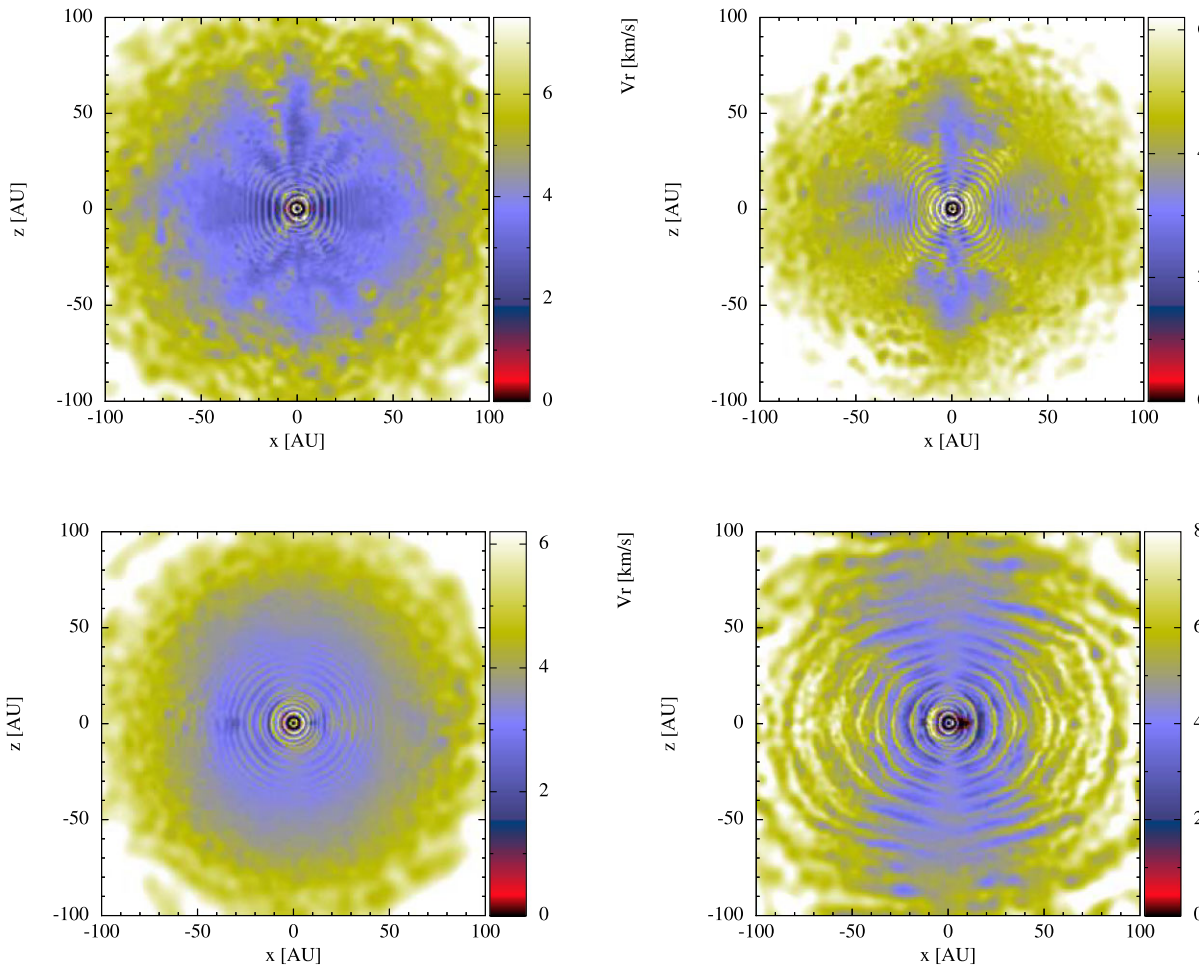
Figure B7. 2D velocity cross-section slices through the x–z plane after ∼ 76 pulsation cycle for models 4 (top left), 9 (top right), 21 (bottom left), and 26 (bottom right).
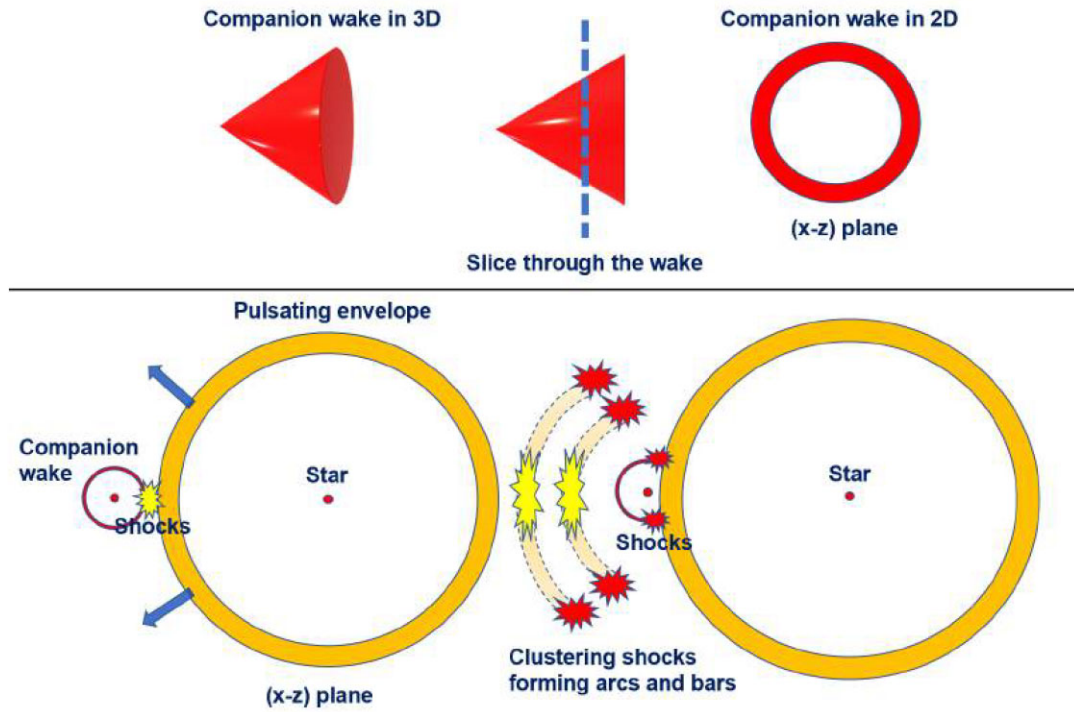
Figure B8. Top: Schematic illustration of the wake of the companion in 3D, showing a cone-like structure and a 2D cross-section slice through the wake forming a circle-shape in the x–z plane. Bottom: Cartoon model (sizes not to scale) illustrating the formation of arcs and bars in the x–z plane due to the shocks between the stellar pulsations and the wake of the companion. The pulsation amplitude is highest when meeting the upper and lower edges of the wake creating stronger shocks that cluster into bars.
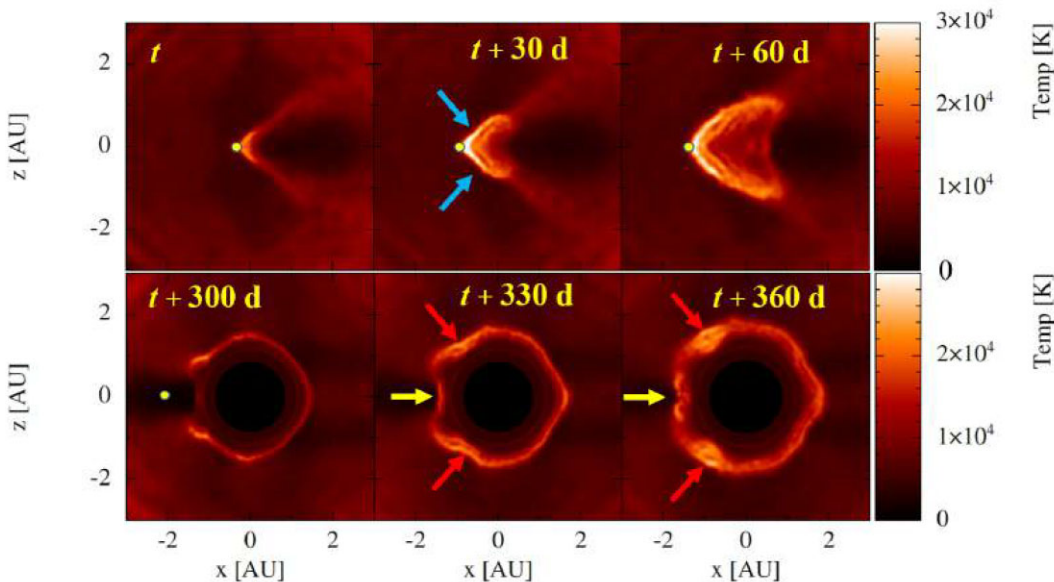
Figure B9. Top: 2D temperature cross-section through the x–z plane at $y = 1.5$ AU and at different time-steps, showing the wake of the companion (blue arrows), forming a cone-like structure in 3D (V-shape in 2D). The yellow dots represent the location of the companion. The cross-section does not show the stellar atmosphere which is at $y \approx 0$. Bottom: 2D temperature cross-section through the x–z plane at $y = 0$ and at different time-steps, showing the shocks between the wake of the companion (a circle in this case; see Fig. B8) and the stellar pulsations. The shocks are highlighted in yellow and red arrows, and they eventually cluster into X-shaped arcs and bars. The companion is moving towards the inside ($y<0$) of the x–z plane.
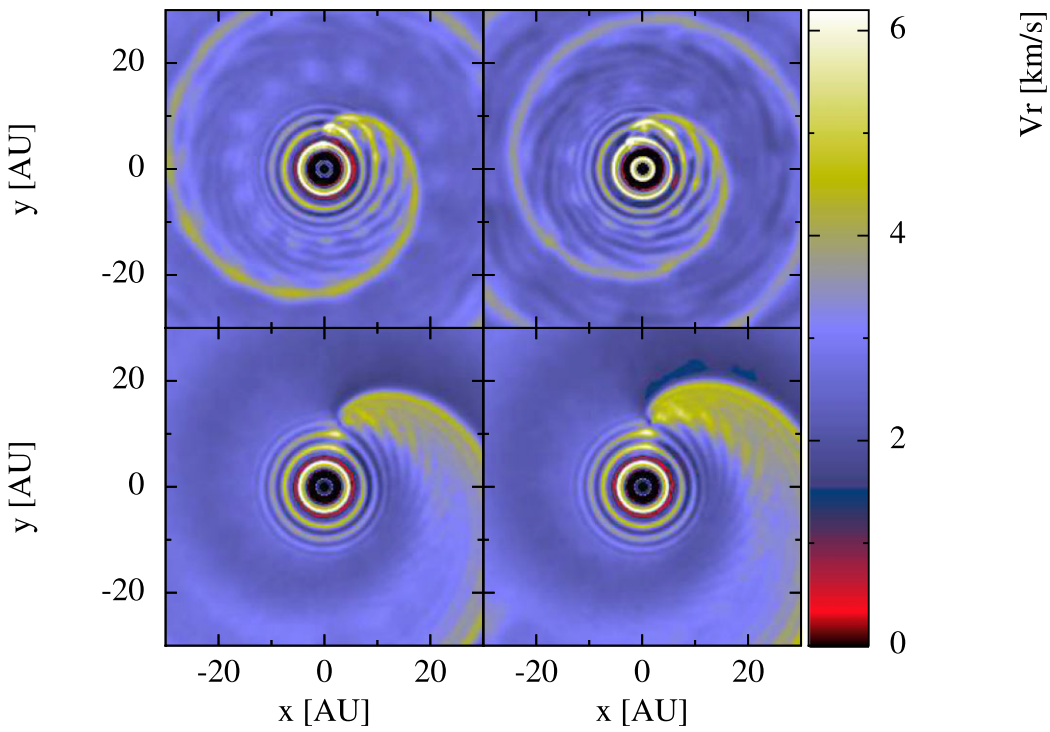
**Figure B10.** Same as Fig. 10 but zoomed-in on the inner region of the spiral arms.
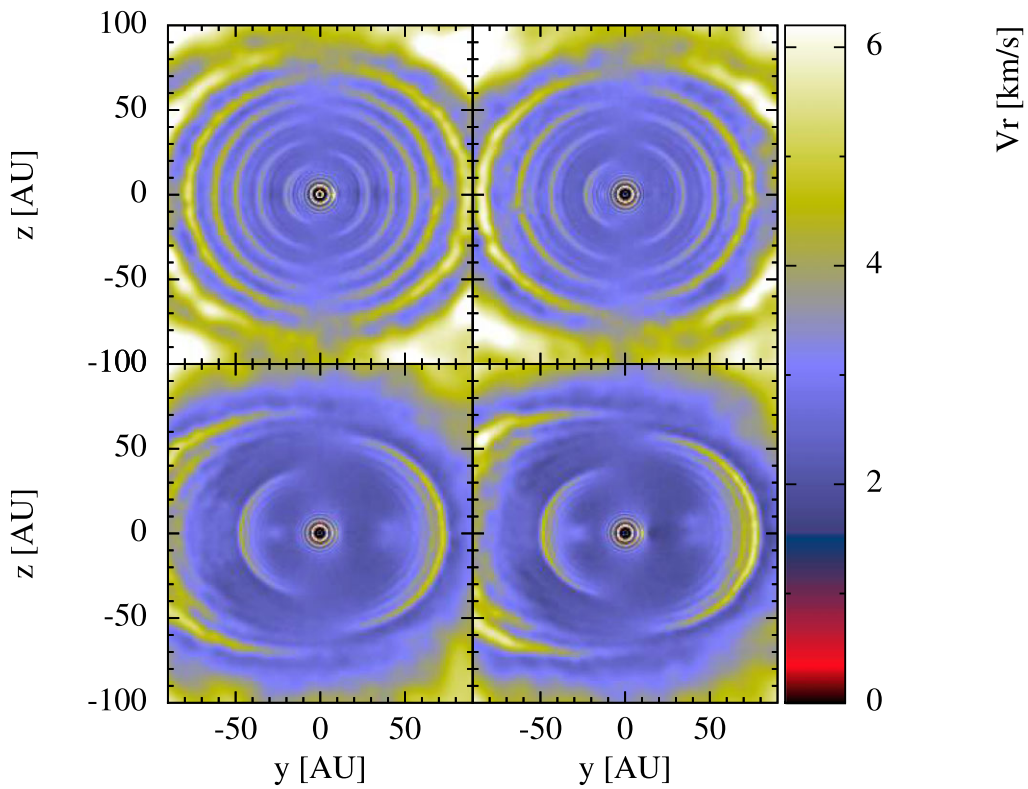
Figure B11. Top: 2D radial velocity cross-section in the y–z plane from models 33 (left-hand panel) and 36 (right-hand panel), after ≈ 76 pulsation cycles. Bottom: same for models 39 (left-hand panel) and 40 (right-hand panel), after ≈ 89 pulsation cycles.
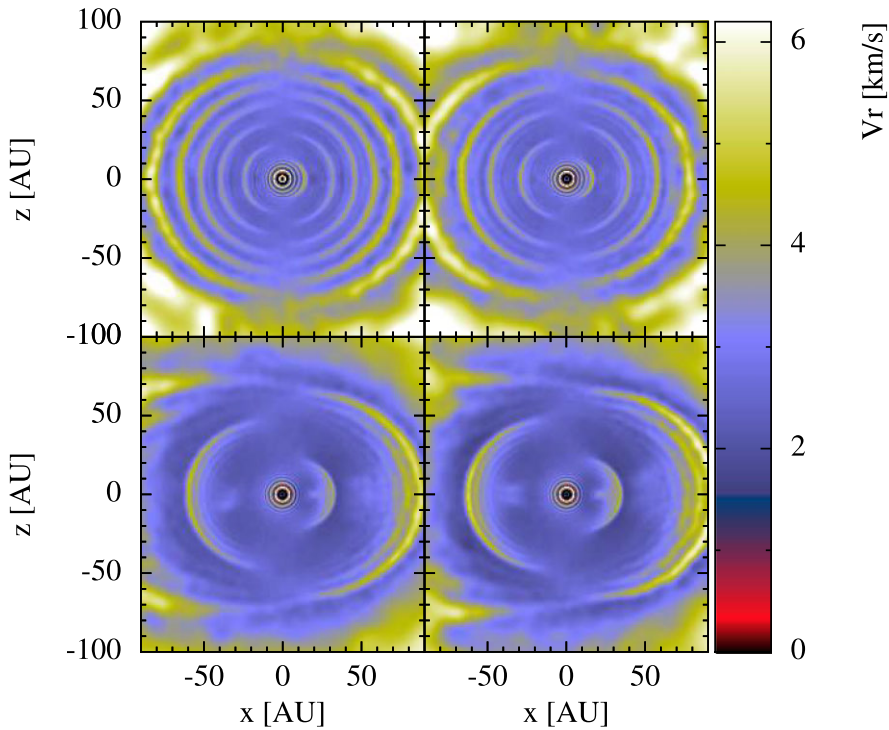
Figure B12. Top: 2D radial velocity cross-section in the x–z plane from models 33 (left-hand panel) and 36 (right-hand panel), after ≈ 76 pulsation cycles. Bottom: same for models 39 (left-hand panel) and 40 (right-hand panel), after ≈ 89 pulsation cycles.
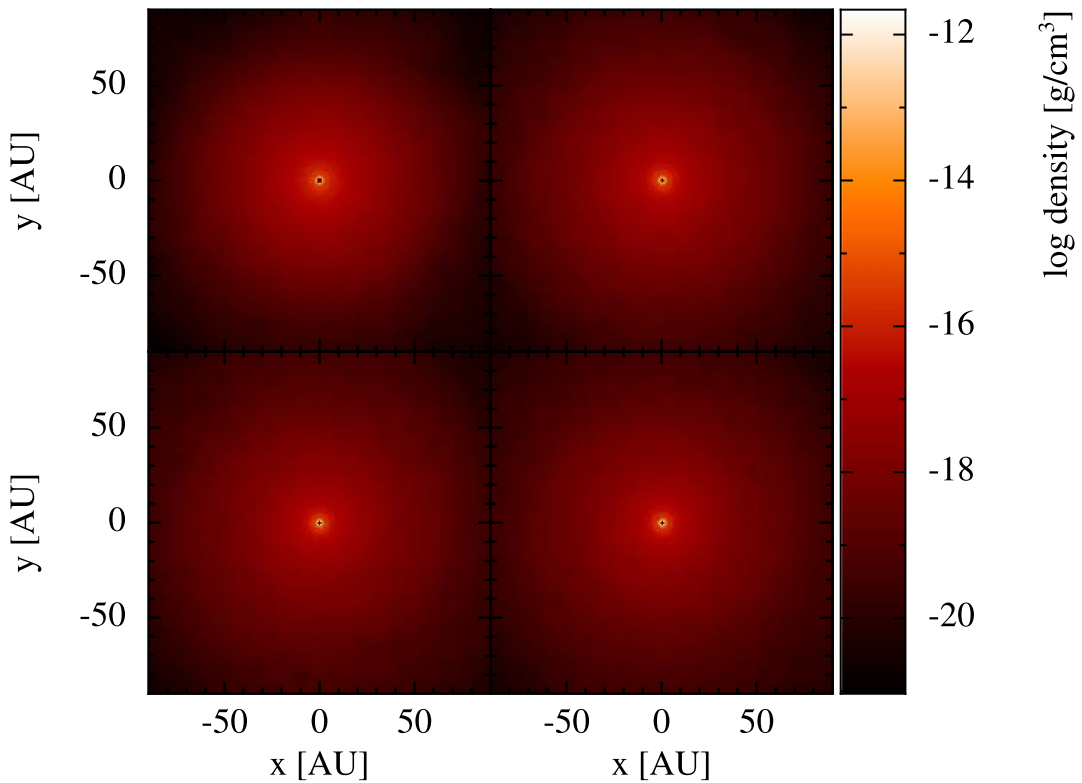

Figure B13. 2D density cross-section through the orbital plane from model 9 after 76 pulsation cycles, but using different resolutions. The models from left to right, top to bottom have the following number of particles: 2.1×10^5, 1.1×10^6, 4.2×10^6, and 8.5×10^6, respectively.

This paper has been typeset from a T$_{\rm E}$X/L$^{\rm A}$T$_{\rm E}$X file prepared by the author.